

Recent Progress in the Development of Semiconductor-Based Photocatalyst Materials for Applications in Photocatalytic Water Splitting and Degradation of Pollutants

Francis Opoku, Krishna Kuben Govender, Cornelia Gertina Catharina Elizabeth van Sittert, and Penny Poomani Govender*

Photocatalytic approaches in the visible region show promising potential in photocatalytic water splitting and water treatment to boost water purification efficiency. For this reason, developing cost-effective and efficient photocatalysts for environmental remediation is a growing need, and semiconductor photocatalysts have now received more interest owing to their excellent activity and stability. Recently, several metal oxides, sulfides, and nitrides-based semiconductors for water splitting and photodegradation of pollutants have been developed. However, the existing challenges, such as high over potential, wide band gap as well as fast recombination of charge carriers of most of the semiconductors limit their photocatalytic properties. This review summarizes the recent state-of-the-art first-principles research progress in the design of effective visible-light-response semiconductor photocatalysts through several modification processes with a focus on density functional theory (DFT) calculations. Recent developments to the exchange-correlation effect, such as hybrid functionals, DFT + U as well as methods beyond DFT are also emphasized. Recent discoveries on the origin, fundamentals, and the underlying mechanisms of the interfacial electron transfer, band gap reduction, enhanced optical absorption, and electron–holes separation are presented. Highlights on the challenges and proposed strategies in developing advanced semiconductor photocatalysts for the application in water splitting and degradation of pollutants are proposed.

1. Introduction

Today, the urgent demand for clean water sources due to the rapid progress in urbanization, industrialization, and huge rises in population has attracted great consideration all over the world. These rapid changes have resulted in environmental problems, such as contaminated air and groundwater as well as hazardous wastes. The increasing demand for fresh water is envisaged to worsen because of the constant release of pollutants and contaminants into the natural water resources. The recycling and reuse of wastewater effluents are important to increase the insufficient supply of clean water.^[1] Previously, several approaches, such as adsorption,^[2] biological treatment,^[3] membrane-based separations,^[4] and chemical treatment,^[5] have been carried out to set up a reliable water treatment. Biological treatments which were traditionally developed to effectively remove the various types of contaminants from water eventually resulted in the production of secondary pollutants, such as soluble refractory organic


compounds as well as health-threatening bacteria which are difficult to remove.^[6] Therefore, the development of a green, sustainable, and nondestructive technology for water/wastewater treatment is of great importance. Semiconductor-based photocatalysts have been one of the most successful approaches for water/wastewater treatment, due to their high efficiency and great potential to remove harmful bacteria and organic pollutants using sunlight.^[7]

To develop efficient semiconductor-based photocatalyst materials for water splitting as well the photodegradation of pollutants in water/wastewater, the optical, electronic, and structural properties of the material have to be carefully investigated. Generally, other features such as morphological architecture, the choice of the semiconductor materials and surface properties should be considered when designing a stable and efficient visible-light-responsive photocatalyst material.^[8] In order to design more efficient semiconductor photocatalysts, first-principles

F. Opoku, Dr. P. P. Govender
Department of Applied Chemistry
University of Johannesburg
P. O. Box 17011, Doornfontein Campus
2028 Johannesburg, South Africa
E-mail: pennyg@uj.ac.za

Dr. K. K. Govender
Council for Scientific and Industrial Research
Meraka Institute
Center for High Performance Computing
15 Lower Hope Road, Rosebank, Cape Town 7700, South Africa

Dr. C. G. C. E. van Sittert
Research Focus Area for Chemical Resource Beneficiation
Laboratory of Applied Molecular Modelling
North-West University
Potchefstroom 2520, South Africa

 The ORCID identification number(s) for the author(s) of this article can be found under <https://doi.org/10.1002/adsu.201700006>.

DOI: 10.1002/adsu.201700006

approaches have been a useful tool in providing a deep understanding of photocatalysis, explaining experimental data as well as predicting novel semiconductor photocatalyst materials with superior performance. In the sections that follow, focus is placed on the recent first-principles based research progress in visible-light-induced photocatalytic activity on semiconductor-based photocatalyst for environmental remediation process. Much emphasis has been focused on the emerging approaches and the fundamental mechanisms of photocatalytic enhancement of doped, nanocarbon, and nanostructuring semiconductor-based photocatalyst materials. This review provides an in-depth knowledge of the fundamental mechanism and understanding of the interfacial electron transfer process that is useful to aid an experimentalist to design and fabricate novel photocatalysts to expand their applicability.

2. First-Principles Methods

Due to the increasing computational power, a theoretical description of processes occurring at the photocatalysts surface is necessary to explore the electronic and optical properties. Therefore, new methods are continuously being designed and applied to address issues related to photocatalysis.^[9] Computational methods, such as quantum Monte Carlo (QMC),^[10] coupled cluster,^[11] and configuration interaction^[12] have been developed to study extremely high accuracy molecular reactions. However, for reactions occurring at solid surfaces and photocatalysis, the method of choice is density functional theory (DFT). Recently, there has been a significant development in the theoretical description of adsorption and reaction occurring at the surface of metal, semiconductor and insulator with DFT.^[13]

To understand and design new photocatalyst materials, it is important to know their electronic structure. Optical and magnetic properties may be explained based on the electronic structure. First-principles calculations allow researchers to explore the nature and origin of the structural, optical, and electronic properties of photocatalyst materials without experimental input. This approach makes use of quantum mechanics as the only basis to calculate electronic states from the atomic species and their positions, without relying on empirical parameters determined by experiment. Sometimes the atomic positions are explored by searching for the minimum-energy configurations. With first-principles calculation, unknown materials can be successfully designed and simulated since empirical parameters are explicitly not required. Therefore, first-principles calculation can be utilized not only to complement existing materials but also as a significant tool for semiconductor-based photocatalyst materials design, such as predicting the physical properties of unknown semiconductor-based photocatalyst materials with the optimal composition to narrow down the search for the most promising photocatalyst materials. Most of the first-principles studies on photocatalysis normally make use of DFT approach to account for the electronic density.^[14] The combination of DFT with projector augmented wave (PAW) approach or pseudopotential, is the most widely used first-principles approach for electronic and optical calculations. Moreover, the term first-principles calculation is often synonymous with DFT. In the



Francis Opoku received his B.Sc. (Hons) Chemistry (2010) and M. Phil. Inorganic Chemistry (2014) degrees from the Kwame Nkrumah University of Science and Technology, Ghana. He is now pursuing a Ph.D. degree in Chemistry under the supervision of Dr. Penny Poomani Govender, Dr. Krishna Kuben Govender, and Dr. Cornelia Gertina Catharina Elizabeth van Sittert in the Department of Applied Chemistry, University of Johannesburg, South Africa. His research interests include the design of efficient semiconductor-based photocatalyst materials and their applications in water splitting as well as degradation of pollutants in wastewater/water resources.



Krishna Kuben Govender obtained his Ph.D. in Computational Chemistry at the University of Cape Town, South Africa in 2014. He then served as a Postdoctoral Research Fellow in 2015 within the Scientific Computing Research Unit at the University of Cape Town. He is currently a Senior Research Scientist at the Center for High Performance Computing, South Africa. His research interests are in quantum mechanics, bioorganometallic chemistry, and hybrid quantum-classical methods.



Penny P. Govender is a senior lecturer in the Department of Applied Chemistry, University of Johannesburg. Dr. Govender received her Ph.D. in 2013 at the University of the Witwatersrand, South Africa. She has extensive experience in academia and is currently the Molecular Modelling Group leader and Head of Department, Applied Chemistry. Her research areas include bioinorganic, computational chemistry, numerical modeling, quantum chemistry, and material science.

past, the issue of high computational costs, which was making it difficult to simulate systems having a large number of atoms had been addressed due to the improvement of computing hardware speed and advances in computational algorithms

designed to take care of computer architectures with higher degrees of parallelism.

Kohn and Sham^[15] established the Kohn–Sham approach to account for the real systems with similar electronic density using an imaginary system of the electrons to account for the noninteracting orbitals. In this approach, exchange–correlation (XC) functional was employed to account for the energy induced by the electron interaction.^[16] Among the several forms of XC functional that have been used in photocatalysis, the generalized gradient approximation (GGA)^[17] and the local density approximation (LDA)^[15] are the most common ones. GGA functionals, such as Perdew–Wang91 (PW91),^[18] Perdew–Burke–Ernzerhof (PBE)^[19] and revised PBE^[20] are available. LDA strongly overestimates adsorption energies and bond strengths, while GGA functionals agree well with experimental data. Moreover, both GGA and LDA fail to describe defect states and typically underestimate the band gap of semiconductor photocatalyst materials. However, the performance of GGA and LDA functionals are generally good for structure calculation.^[21] In addition, LDA functionals normally underestimate the lattice constants calculation by 1%–2% compared to the experimental data. Furthermore, GGA functionals normally produce larger lattice constants than the LDA functionals and in some cases overestimate the lattice constants of materials to a significant extent.^[22]

To account for the band gap underestimation and lattice constants overestimation, several approaches, such as the DFT + U, hybrid functionals, quasiparticle GW approximation (GWA) and other methods have been developed. The Heyd–Scuseria–Ernzerhof (HSE) hybrid functional^[23] have successfully overcome the band gap underestimation issues by mixing the PBE functional with the Hartree–Fock (HF) wave function. The PBE and PW91, as well as hybrid functionals, such as HSE06 and PBE0, are the most popular for materials calculations.^[24] The significant difference between PBE0 and PBE is the substitution of the PBE functional by the exact HF exchange.^[19] The HSE03 and HSE06 functionals were designed to address the expansive HF calculations, where the short range interaction was described by the HF exchange.^[25] The percentage of HF wave function in the HSE functional is not a constant and the optimum value depends on the nature of the system. Since the Kohn and Sham DFT calculation is less suited to analyze strongly correlated electron systems with localized electrons, adding a Hubbard parameter (U) to GGA or LDA (DFT + U) calculation can also improve the band structure depending on the choice of several empirical parameters.^[26] In this approach, electrons are divided into itinerant electrons (electrons with s and p atomic orbital) and localized electrons (electrons with d and f atomic orbital). The DFT + U approach uses DFT approach for the s and p electrons with the HF wave function approach for the d and f electrons. The HF wave function approach makes use of an approximation to consider the on-site interactions with the interatomic interactions ignored. The DFT + U approach take appropriate description for the localized and strongly correlated electron system due to the consideration of the electronic interactions of the d and f electrons as an intrinsic part of the electronic system. The DFT + U approach make use of the effective interaction parameter (U_{eff}) with the on-site interactions for the localized d and f electrons. The U_{eff} parameter obtained

empirically from the difference of the parameter for Coulomb interaction between electrons (U) and the exchange interaction parameter (J). The parameter-free first-principles GWA gives a precise information on the electronic structure, however, at the expense of computational cost.^[27] The name “GW” comes from the Green’s function (G) and the dynamically screened Coulomb potential (W).^[28] To enhance the electron correlation effect, other approaches, such as QMC, dynamical mean-field theory (DMFT) and Moller–Plesset (MP2) have been developed. The MP2 approach is used for cluster calculation,^[29] while the DMFT and QMC approaches are computationally demanding for complex-structured calculation.^[30] In addition, this high-level HSE hybrid functional and GWA approaches are much more reliable compared to the GGA and LDA functionals, but currently, their computational cost does not allow their application in complex structure systems. The calculations for organic molecules differ from the inorganic materials with the periodic boundary conditions and nonlocalized plane wave basis sets instead of the localized Gaussian-type basis sets for the inorganic materials.

The most commonly used calculation programs for materials calculations are the Vienna Ab initio Simulation Package package (VASP), Spanish Initiative for Electronic Simulations with Thousands of Atoms (SIESTA), Quantum espresso, DMol³ and Cambridge Serial Total Energy Package (CASTEP).

VASP is a computer program for atomic scale materials modeling for quantum-mechanical molecular dynamics and electronic structure calculations using a plane wave basis set and either PAW method or Vanderbilt pseudopotentials to describe the electron–core interaction.^[31] VASP computes an approximate solution to the many-body Schrödinger equation, either within HF approximation to solve the Roothaan equations or DFT to solve the Kohn–Sham equations. The performance of VASP for solid-state, molecular, polymer, and surface applications is similar to Gaussian type implementations of DFT. The basic method is DFT, however, the VASP code utilized post-DFT corrections, such as HF exchange, many-body perturbation theory, hybrid functionals and dynamical electronic correlations within the random phase approximation. VASP code is applied in phase and structure stability, dynamical and mechanical properties, glasses, liquids and quasicrystals, magnetic nanostructures, semiconductors and insulators, interfaces, surfaces, and thin films, chemical reactions as well as photocatalysis.

SIESTA is a method and software implementation for performing electronic structure calculations and ab initio molecular dynamics simulations of solids and molecules.^[32] SIESTA uses a DFT code, such as Kohn–Sham band structures, Mulliken populations, and electron density to predict the physical properties of atoms. SIESTA program is applied in geosciences, materials physics and chemistry, engineering, and biology.

CASTEP is a state-of-the-art quantum mechanics-based program specifically designed for solid-state materials science, solid-state physics, chemistry, and chemical engineering where empirical models and experimental data may be sparse.^[33] CASTEP employs the DFT plane-wave pseudopotential method to explore the properties of surfaces and crystals in materials, such as metals, semiconductors, ceramics, zeolites,

Table 1. The band gap, CB (E_{CB}) and VB (E_{VB}) edge positions of commonly used semiconductors at pH zero versus normal hydrogen electrode (NHE) (Adapted with permission^[36]). (E_{CB} – conduction band edge, E_{VB} – valence band edge.).

| Photocatalyst | Band gap [eV] | E_{CB} [eV] | E_{VB} [eV] | References |
|--------------------------------|---------------|------------------|------------------|---------------------------------------------------------------------------------------------------------------------------|
| Fe ₂ O ₃ | 2.00–2.20 | 0.30–0.60 | 2.40–2.70 | Barroso et al., ^[37] Huda et al., ^[38] van de Krol et al. ^[39] |
| TiO ₂ (rutile) | 3.00–3.70 | –0.05–0.15 | 2.92–2.95 | Aragaw et al., ^[40] Alonso et al., ^[41] Scanlon et al., ^[42] Luan et al. ^[43] |
| TiO ₂ (anatase) | 3.20 | –0.10 | 3.10 | Hernández-Alonso et al., ^[41] Scanlon et al. ^[42] |
| WO ₃ | 2.60–2.80 | 0.24, 0.40, 0.73 | 2.99, 3.20, 3.45 | Bledowski et al., ^[44] Wang et al., ^[45] Liu et al. ^[46] |
| BiVO ₄ | 2.40 | 0.46 | 2.86 | Ding et al. ^[47] |
| ZnO | 3.20, 3.30 | –0.25, –0.20 | 2.95, 3.10 | Huang et al., ^[48] Lee et al. ^[49] |
| Si | 1.10 | –0.25 | 0.85 | Chen et al., ^[50] Tran et al. ^[51] |
| Ta ₃ N ₅ | 2.10 | –0.55, –0.53 | 1.55, 1.57 | Chen et al., ^[50] Hisatomi et al. ^[52] |
| TaON | 2.40 | –0.40, –0.35 | 2.00, 2.15 | Chen et al., ^[50] Hisatomi et al. ^[52] |
| MoS ₂ | 1.73 | –0.04 | 1.69 | Pan et al. ^[53] |
| CuO | 1.55 | –0.51 | 1.04 | Nakaoka et al. ^[54] |
| GaAS | 1.40 | –0.40 | 1.00 | Grätzel ^[55] |
| Cu ₂ O | 2.00 | –0.70 | 1.30 | Paracchino et al. ^[56] |
| GaP | 2.25 | –0.71 | 1.54 | Liu et al. ^[57] |
| CdSe | 1.70 | –0.54 | 1.16 | Kudo et al. ^[58] |
| SiC | 3.26 | 2.99 | –0.27 | Kim et al. ^[59] |
| CdS | 2.40 | –0.50 | 1.90 | Kohtani et al. ^[60] |

and minerals. CASTEP can also study the spatial distribution of charge density, as well as point and extended defects in semiconductors.

DMoL³ is a modeling program, which uses DFT to predict properties of materials and simulate chemical processes both accurately and rapidly.^[34] Since DMoL³ can predict processes in solid, solution and gas-phase environments, chemistry, solid-state physics, pharmaceuticals, chemical engineering, and materials science. DMoL³ are used to investigate the origin and nature of structural and electronic properties without experimental input.

Quantum ESPRESSO is an integrated suite of open-source computer codes for electronic-structure calculations and materials modeling at the nanoscale based on DFT, pseudopotentials, and plane waves. The Quantum ESPRESSO distribution comprises a core set of components and plug-ins to perform advanced tasks, as well as a number of third-party packages designed to be inter-operable with the core components.

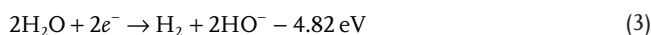
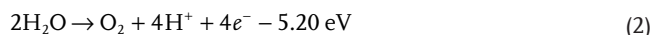
3. Semiconductor-Based Photocatalyst

Photocatalytic water splitting, using sunlight for oxygen (O₂) and hydrogen (H₂) production and photodegradation of pollutant, is envisaged as a promising approach to solve environmental issues.^[35] To effectively develop a semiconductor photocatalyst capable of employing sustainable and safe solar energy, several preconditions need to be fulfilled: (i) lower band gap to absorb a wider fraction of the solar energy; (ii) long-term stability, nontoxic, low cost, chemically and biologically inert; (iii) effective mobility of the photogenerated charge carriers; and (iv) appropriate CB and VB alignment with reference to the water reduction (E_{H_2/H^+}) and oxidation (E_{O_2/H_2O}) potential, respectively to meet water splitting thermodynamic criterion.

Table 1 shows the band gap, CB and VB edge positions of commonly used semiconductor-based photocatalysts.

The band gap, the VB and CB edge positions of semiconductors are the two most essential parameters, which mostly determine their photocatalytic activity under simulated sunlight irradiation. The VB and CB edges of commonly used semiconductors^[36] with reference to E_{H_2/H^+} and E_{O_2/H_2O} potentials are given in **Figure 1**.

If E_{CB} is positioned more negative than the E_{H_2/H^+} potential and the E_{VB} is also aligned more positive than the E_{O_2/H_2O} potential, then the water molecule can split into H₂ and O₂ under sun light irradiation.^[61] The photocatalytic water splitting reactions are a thermodynamically uphill route, which requires an energy of 1.23 eV versus normal hydrogen electrode (NHE) as well as high over potentials due to its nonspontaneous process with a $\Delta G^\circ = 237.2 \text{ kJ mol}^{-1}$ (2.46 eV vs NHE) per H₂O molecule.^[52] In electrochemistry, over potential is the potential difference between the potential at which the redox reactions are experimentally determined and the thermodynamically observed reduction potential.^[62] The 1.23 eV versus NHE in Equation (1) arises from the corresponding oxidation (Equation (2)) and reduction (Equation (3)) of water^[61]



The oxidation and reduction reactions are the basis of photodegradation of organic pollutants and photocatalytic H₂ production, respectively.

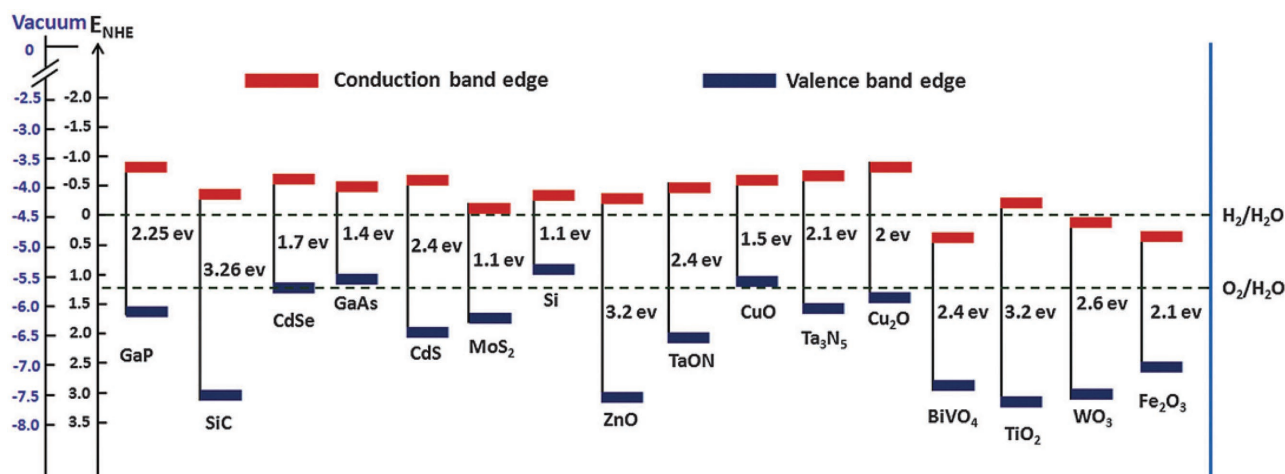


Figure 1. The CB and VB edges of commonly used semiconductors at pH zero with reference to water redox potential. Adapted with permission.^[36] Copyright 2016, Royal Society of Chemistry.

The sequence of chain reactions that normally occur during the photocatalytic process is broadly proposed. Generally, when a semiconductor-based photocatalyst is struck by sunlight, electrons (e^-) and holes (h^+) are generated. Subsequently, the photon absorption and excitation of an electron from the VB to the CB can occur on condition that the incoming photons are either equal to or larger (\geq) than the semiconductor band gap (E_g), leaving behind holes on the VB (Equation (4)) as given in **Figure 2**.



The photogenerated electron-hole (e^-/h^+) pairs might be captured by the semiconductor surface defects sites and undergo recombination and release the remaining energy via a nonradiative mechanism (Equation (5))

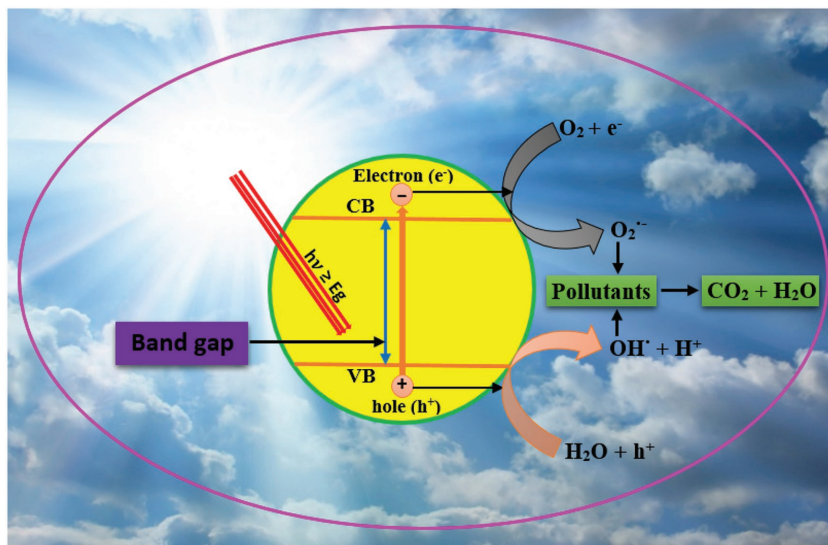
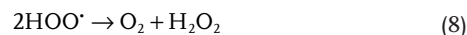
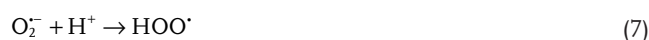
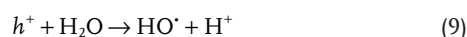


Figure 2. Schematic of semiconductor photocatalysis process.

The defect site on the semiconductor surface reduces the overall performance of the photocatalytic reaction. Accordingly, the photogenerated charge carriers undergo separation and migration to the reaction sites. Later the photoinduced charge carriers partake in the redox reactions if the process is thermodynamically feasible. Herein, the redox reaction normally involves two major active species: superoxide ($O_2^{\cdot-}$) and hydroxyl ($\bullet OH$) radicals. The $O_2^{\cdot-}$ radical is formed when O_2 reacts with the CB photoexcited electron (Equation (6)). The $O_2^{\cdot-}$ can be protonated to form hydroperoxyl radical ($\bullet OOH$) and later peroxide (H_2O_2) (Equations (7) and (8)).^[63]



The generation of hydroxyl radicals normally occurs through two routes, (i) H_2O and OH^- ion in the water environment are easily oxidized by the photogenerated h^+ to generate the $\bullet OH$ radical (Equations (9) and (10)); (ii) H_2O_2 formed in Equation (8) can further decompose to produce $\bullet OH$ radical (Equation (11)). In addition, the h^+ can directly act as an oxidant to degrade the pollutants in the water environments as shown in Equation (12) and their potential depends on the oxidation conditions and catalyst type^[64]



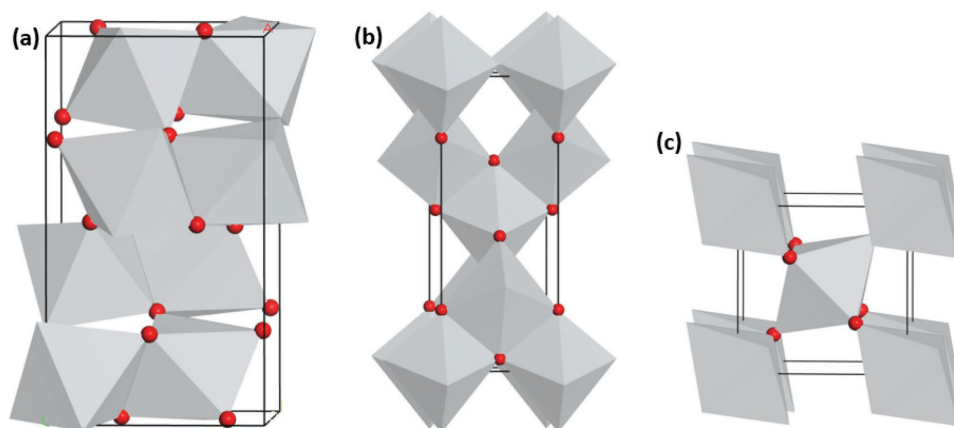
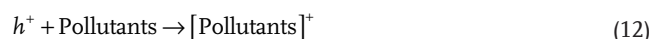
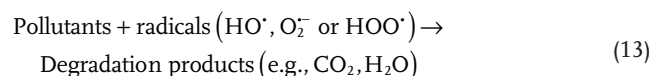


Figure 3. Crystal structures of TiO_2 polymorphs: a) brookite, b) anatase, and c) rutile. The gray octahedral represent TiO_6 blocks and red spheres represent O atoms.



During the photodegradation of pollutants, the $\bullet\text{OH}$ and $\text{O}_2^{\bullet-}$ radicals are the primary oxidants. The $\bullet\text{OH}$, $\text{O}_2^{\bullet-}$, and $\bullet\text{OOH}$ radicals attack the pollutants in the water (Equation (13)), which results in several intermediates based on the nature of the pollutant. The resultant intermediates subsequently react to generate the final degradation products (e.g., CO_2 and H_2O)



When the photocatalytic degradation of pollutants does not proceed simultaneously as expected, electrons accumulate in the CB, which further increases the recombination rate of charge carriers. Thus, the presence of specific scavengers is important to reduce the recombination rates of the charge carriers thereby enhancing the overall photocatalytic performance.

The flow of photogenerated charge carriers toward specific crystal facets enhances the selectivity and reaction efficiency of the photocatalyst. Selectivity is one of the most desired properties of photocatalysts during the degradation process. Selectivity in photodegradation is achieved during the attraction, adsorption and mineralization stages of photocatalysis by adjusting the initial concentration of pollutants, pH of the solution and light intensity,^[65] band gap,^[66] as well as the pore size and surface charge of the photocatalyst.^[67] Selective adsorption of pollutants with charged polarity is primarily evaluated by the charge and size of the exposed surface of the photocatalyst, signifying that Coulombic interactions are vital in the photodegradation of pollutants.^[68] Generally, selectivity is influenced by the oxidation ability of certain reactive species, structure, and components of the photocatalysts.^[69]

To utilize the solar energy for environmental remediation application, it is highly necessary to design a novel semiconductor photocatalyst, which is of high photostability with efficient visible-light absorption. Fujishima and Honda^[70] were the first to report the photocatalytic production of H_2 by splitting

water on TiO_2 electrodes. TiO_2 is the most widely studied photocatalyst due to its effective mobility of the photogenerated electron–hole pairs, nontoxicity, high negative reduction potentials, high stability, eco-friendliness, and cheapness.^[70] TiO_2 exists in three crystalline phases: brookite (Pbca), rutile (P42/mnm), and anatase (I41/amd) (Figure 3).

All the modifications contain TiO_6 octahedral that are interconnected through four (anatase), three (brookite), or two (rutile) shared corners and common edges. Among them, anatase displays better photocatalytic activity.^[71] Since TiO_2 was initially employed as a photocatalyst, hundreds of oxynitride, sulfides, and oxides, such as SnS_2 ,^[72] ZnO ,^[73] BiVO_4 ,^[74] SnO_2 ,^[75] ZnS ,^[76] BiOX ($X = \text{Cl}, \text{Br}, \text{I}$),^[77] AgP_3O_4 ,^[78] Bi_2MO_6 ($M = \text{W}, \text{Mo}$),^[79] H_2WO_4 ,^[80] BiPO_4 ,^[81] ATaO_3 and ANbO_3 ($A = \text{Li}, \text{Na}, \text{and K}$),^[82] ZnSnO_3 ,^[83] RuO_2 ,^[84] IrO_2 ,^[85] LiNbO_3 ,^[86] Ag_3PO_4 ,^[87] AMWO_6 ($A = \text{Rb}, \text{Cs}; M = \text{Nb}, \text{Ta}$),^[88] AgMO_2 ($M = \text{Al}, \text{Ga}, \text{In}$),^[89] ZrO_2 ,^[90] CoS ,^[91] NiS ,^[92] NiS_2 ,^[93] CuS ,^[94] MoS_2 ,^[95] MoS_3 ,^[96] WS_2 ,^[97] AgTaO_3 ,^[98] GaN ,^[99] graphitic carbon nitride (g- C_3N_4),^[100] Ge_3N_4 ,^[101] $\text{Sm}_2\text{Ti}_2\text{S}_2\text{O}_5$,^[102] Ta_3N_5 ,^[103] TaON ,^[104] Fe_3O_4 ,^[105] metal chalcogenides,^[106] SrTiO_3 ,^[107] NiO ,^[108] CuO ,^[109] SrNb_2O_6 ,^[110] $\text{Sr}_2\text{M}_2\text{O}_7$ ($M = \text{Nb and Ta}$),^[111] $\text{Bi}_{12}\text{TiO}_{20}$,^[112] NaNbO_3 ,^[113] AgBr ,^[114] SbMO_4 ($M = \text{Nb}, \text{Ta}$),^[115] $\text{Bi}_{24}\text{Al}_2\text{O}_{116}$ and others have been utilized as a photocatalyst in water purification applications.

The large band gap of some semiconductors, such as TiO_2 (3.0 eV for rutile and 3.2 eV for anatase),^[117] SrTiO_3 (3.25 eV for cubic perovskite),^[118] ZnO (3.34 eV),^[119] BiOCl (3.40 eV),^[120] ZrO_2 (≈ 5.0 eV),^[121] and others,^[122] have limited their application only to the UV region ($\lambda < 400$ nm), which comprises of $\approx 4\%$ of the solar energy. Thus, the band gap has to be narrowed to ≈ 2 eV, for the photocatalyst to utilize the visible light ($\lambda > 400$ nm), which comprises of 43% of the solar spectrum.^[123] Furthermore, the overall low quantum efficiency induced by the fast recombination of the charge carriers, which is common to all semiconductor photocatalysts, is another drawback. Therefore, the search for novel photocatalysts with a visible-light-driven performance that can utilize the full solar energy is highly desirable. As a result of these challenges, a number of approaches such as doping,^[124] structural modification,^[125] quantum dot sensitization,^[126] and semiconductor composite formation^[127] have been developed.

4. Recent Progress in the Design of Semiconductor Photocatalyst Materials

4.1. Doping

Several properties of semiconductor-based photocatalyst materials are controlled by impurities and defects. The synthesis of n- and p-type doped systems motivates the development of visible light photocatalyst materials. To accomplish this development, a comprehensive understanding of factors that control the doping process is essential and first-principles calculation has made a significant contribution to this effect. Several studies have endeavored to identify the fundamental causes of these challenges.^[128] A general conclusion drawn from these studies revealed that n- and p-type doping has been a challenge especially when the energy of the VB maximum (VBM) is low and the CB minimum (CBM) is high on the absolute energy scale. In particular, the introduction of a filled electronic state with a higher energy compared to the CBM energy normally results in electron transferred to the CB. However, when the CBM is higher in energy compared to the energy of the filled electronic state, the variety of impurities that can achieve these effects are limited. Moreover, processes such as atomic relaxation of the impurities away from their substitution sites and spontaneous formation of defects can lower the energy of the electron been added if the energy of the CBM is high.

The properties of functional photocatalyst materials are modified by doping.^[129] The doping effect on the photocatalyst properties depends on the catalyst physicochemical properties, method of fabrication, concentration, and type of dopant.^[130] The introduction of dopants in the crystal lattice of semiconductors result in dramatic changes in their crystal structures, producing either n-type or p-type semiconductors depending on the nature of the impurities. n-Type semiconductors are produced when the impurities are capable of providing extra electrons to the host atom, whilst p-type semiconductors are capable of providing extra valence holes to the host atom. Doping semiconductors with transition metals,^[131] metalloids,^[132] lanthanides,^[133] noble metals,^[134] alkaline-earth metals,^[135] nonmetals,^[136] and rare earth metals^[137] have been efficient strategies to increase the photoresponse toward the visible region and adjust the band structure.

For some semiconductors, the achievement of higher doping levels required for photocatalysis process is difficult. At such high doping levels, not every dopant gives excellent results due to the self-compensation effect. In several cases, this compensation effect is ascribed to the formation of point defect. However, direct experimental studies of defect formation are lacking due to the challenging in instituting quantitative measurement of point defect. First-principles calculation can offer an in-depth knowledge regarding point defect that normally occurs in doping.

4.1.1. Metal Doping

Point defects in semiconductor-based photocatalysts always introduce states or levels near the band edges or in the band gap. These states determine the behavior of electrons and

often used as the identification for experimental points defects. Therefore, the detailed calculation of these states is necessary for the characterization and identification of point defect. For instance, internal excitation of point defects may occur when the defect charge remains unaffected. The introduction of metal ions produces an intraband state close to the VBM or CBM edge to induce visible light optical absorption due to the close range of the redox energy states of several metal ions in the band gap states. The enriched visible light absorption was ascribed to the migration of the charge transfer between the VB (CB) of the semiconductor and the d-electrons of the metal dopant. Moreover, the metal ions can change the equilibrium concentration of the charge carriers by acting as a trap for charge carriers, thereby enhancing the degradation rate.^[138] In the semiconductor band structure, the metal s-, p-, and d-orbitals contribute to the unoccupied CB, while the oxygen 2p orbitals contribute to the filled VB. The metal d-orbitals dominate the lower position of the CB.^[139] Noble metal doped semiconductors have been shown to expedite the transfer of photogenerated charge carriers, as well as improving its visible light photoelectron conversion efficiency, owing to their surface plasmon resonance effect.^[140] For example, Ru,^[141] Rh,^[142] Pd,^[143] Pt,^[144] Au,^[145] and Ag^[146] have been shown as efficient cocatalysts for photocatalytic water splitting and degradation of organic pollutants. Among them, Pt has been the most efficient cocatalyst owing to its low overpotential and high work function for environmental radiation process.^[147] Moreover, some low-cost transitional and earth-abundant metals, such as Co,^[148] Ni,^[149] and Cu,^[150] have also been explored as efficient cocatalysts. An impurity level may be introduced into the forbidden band upon metal doping based on the oxidation states and ionic radius of the host and dopant atoms. An impurity level is the energy band that are unoccupied by electrons. This impurity level may serve as either an electron donor or acceptor by allowing the semiconductor to absorb visible light and as a result, several visible light photoresponse by cation dopant have been reported.^[151] In principle, the Kohn–Sham approach that results from electronic structure calculation, in particular, band gap determination cannot be directly measured with any levels that are significant for experimental studies. Therefore, the total energy of defect configuration before and after the migration needs to be considered. All-electron calculations can be obtained with approaches, such as atom centered basis sets and full-potential linearized augmented plane-wave (LAPW) approach.^[152] Moreover, the approximate treatment of the core electrons are normally determined using the PAW^[153] and pseudopotential approaches.^[154] PAW is an enhancement to the pseudopotential approach since it combines the pseudopotential approach with the LAPW method, making PAW more accurate compared to the pseudopotential approach. These approaches have been applied to large system, in particular, first-principles calculation of point defect with computationally controllable systems compared to the other all-electron approaches. The pseudopotential and PAW approach for the core electrons treatment can be achieved with the plane-wave and pseudoatomic orbital basis sets.^[155]

Transition metal-doped TiO₂ can produce impurity levels in the forbidden band, which may influence the enhanced visible light absorption, but the underlying mechanism remains

unclear. The introduction of lanthanide ion into TiO_2 enhanced its visible light optical absorption compared to the pure TiO_2 . This study was done using LDA functional and PAW method with Hubbard U correction (LDA + U) due to the inaccurate description of the 4f orbitals of lanthanide using standard DFT.^[156] In this system, a U parameter of 10 and 5 eV for Ti 3d and O 2p orbitals reproduce the experimental band gap of TiO_2 . The extra electronic states introduced into the band gap contributed to the improved red shift of TiO_2 doped with Fe^{3+} via B3LYP functional with double-zeta LanL2DZ basis set.^[157] Within plane-wave pseudopotential DFT approach, Fe^{3+} ion in TiO_2 bulk was localized and mainly act as the recombination centers of the photoinduced holes and electrons, which is beneficial to photocatalysis.^[158] The ultrasoft pseudopotential and GGA of PBE functional were used to account for the electron–ion interaction and the exchange–correlation effect, respectively. In addition, the photocatalytic activity of Fe-doped TiO_2 decreases as the dopant concentration increase, which was ascribed to the reduced recombination rate of the charge carriers. The accumulation of more positively charged holes contributed to the improved photocatalytic performance of Pt-doped TiO_2 via first-principles calculations with ultrasoft pseudopotential and plane-wave basis sets implemented in CASTEP code of Materials Studio.^[159] The Pt-doped TiO_2 showed an excellent photocatalytic degradation activity toward nitrobenzene with respect to the pure Pt clusters. In addition, recent studies on the optical properties and electronic structure of Cu-doped TiO_2 revealed an induce doping states, which comprise of Cu 3d and Ti 3d state near the VBM and this state improves the visible light absorption ($\lambda = 400\text{--}1000$ nm).^[160] Through periodic DFT approach and PAW method, Cu-doped TiO_2 showed a covalent character in the Cu–O bond as well as new states in the VBM, which reduced its band gap.^[161] For this systems, a DFT + U ($U = 5$ eV) approach was used to account for the Coulomb interaction. The exchange–correlation effect was treated within the LDA and PBE functional. In addition, the lattice constant and atomic positions were optimized with the conjugate-gradient method. The introduction of Cu into TiO_2 produces new states at the VBM, which mainly comprises of Cu 3d and O 2p states. Based on first-principles DFT calculation with PBE parameterization of GGA functional for the exchange and correlation effects, the improved visible light photocatalytic performance of Ni-doped TiO_2 was due to the forbidden gap impurity energy levels, which was introduced between the CB and VB.^[162] In addition, the band gap was observed to have increased by 0.1 eV compared to the bulk TiO_2 with Ni 3d states within the band gap owing to its stronger interactions with O 2p state. The excitation of the occupied Ni 3d state to its CB decreases the photon excitation energy and induces enhanced photocatalytic performance. This study explains the experimentally observed enhanced photocatalytic performance of Ni-doped TiO_2 . Through DFT calculation with plane-wave pseudopotential approximation, the nature of the n-type of Mo-doped TiO_2 was found to contribute to the states created by the Mo dopant below the CB and the Fermi level in the CB (Figure 4).^[163] The interactions between the ionic core and valence electrons were described using ultrasoft pseudopotential along with PBE functional. All the systems were optimized by the Broyden–Fletcher–Goldfarb–Shanno algorithm with a self-consistent field of 10^{-6} eV per atom.

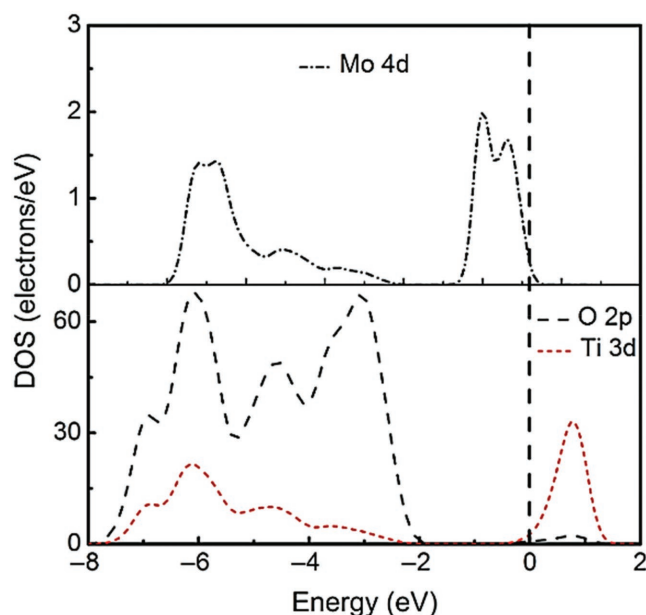


Figure 4. Partial density of states (PDOS) of Mo- TiO_2 . Adapted with permission.^[163] Copyright 2014, American Scientific Publishers.

The Cr impurity at Ti sites was observed to influence the visible light photocatalytic performance of Cr-doped SrTiO_3 based on DFT study as implemented in VASP code with HSE hybrid functional.^[164] Bismuth vanadate (BiVO_4) has received a considerable attention as a promising photocatalytic material. Recently, the behavior of an excess electron in BiVO_4 was investigated using the hybrid DFT method with varying fraction of the HF exchange.^[165] This studies revealed that the photocatalytic activity and electron mobility of the bulk mBiVO_4 were moderately low owing to the excess electron mainly localized on the V atom. In addition, the poor mobility of electrons in mBiVO_4 was owned to the poor overlap of V 3d orbital with Bi 6p orbital at the CBM.^[166] An efficient route to enhance the photocatalytic performance and electron mobility of mBiVO_4 involves the modification of its electronic structure with other elements. To explore the photocatalytic performance of doped BiVO_4 , the optical properties and electronic structures were calculated using DFT method. The effects of Au, Ag, and Cu on the photocatalytic performance of BiVO_4 was studied based on ab initio molecular dynamics method with GGA functional of PW91 for the exchange–correlation effects and plane-wave pseudopotential approximation to address the electron effect.^[167] For Cu-doped BiVO_4 system, the occurrence of Cu 3d acceptor state reduce the band gap and enhance the separation of the photoinduced electron–hole pairs by acting as a trap to the photoexcited electrons. The improved photocatalytic activity of Cu-doped BiVO_4 was ascribed to its smaller effective mass and the acceptor state. Through DFT studies, surface properties of Mo-doped mBiVO_4 was investigated to comprehend the origin of the improved photocatalytic activity.^[168] The improved photocatalytic performance of Mo-doped monoclinic BiVO_4 was ascribed not only to the facilitated separation of the photoinduced electron–hole pairs but also to the surface oxygen quasi-vacancies using hybrid HSE06 functional and ultrasoft

pseudopotentials method for the ion cores interaction.^[168] In addition, BiVO₄ doped with Mo does not result in band gap reduction but rather reduction in the effective mass of holes.^[169] The ultrasoft pseudopotential used in this calculation was due to its velocity and efficiency. The valence electrons of the Kohn–Sham wavefunctions were described using plane wave basis set with a cutoff energy of 380 eV. The optical absorption spectra of Ag/Bi₂WO₆ (001) nanocomposites revealed an obvious red-shift visible light absorption as the concentration of Ag increases.^[170] Silver halide materials have been applied in photocatalysis with an extraordinary stable and higher performance compared to the most widely used TiO₂. The crystal field splitting of Ag 4d states in the VB of AgX (X = Cl, Br, I) was the main factor influencing the large effective mass of the photoinduced holes via LDA functional and PAW approach.^[171] In addition, the smaller effective mass of the photoinduced electrons at the CB minimum (CBM) contributed to the improved photocatalytic activity of AgX (X = Cl, Br, I).

4.1.2. Nonmetal Doping

Doping semiconductors with transition metals could effectively enhance visible-light photoresponse, but it is at the cost of reduced thermal stability and efficiency.^[172] Another approach to prolong visible light absorption of semiconductors is nonmetal doping. Nonmetal doping has been largely known to sensitize semiconductors toward visible light region as opposed to surface sites known to trap photogenerated e^-/h^+ pairs by metal dopants.^[173] Nonmetal dopants can behave as part of the VB or create electronic states near the VB, thereby narrowing the band gap of the semiconductor.^[174] Asahi et al.^[129] were the first to investigate N-doped TiO₂ using a sputtering nitrogen-containing gas mixture and their results showed an enriched visible light absorption. The improved red shift of N-doped TiO₂ was found to be attributed to N 2p levels close to the VB.^[175] Other researchers have also confirmed similar results when Titania was doped with N.^[176] Likewise, other nonmetals, such as C,^[177] S,^[178] and F^[179] have also been introduced into the semiconductor lattice. The nonmetal doping effect of semiconductor materials on the optical property and electronic structure has been theoretically evaluated.^[180] Currently, transition metal tungsten oxide-based (AMWO₆ (A = Rb, Cs; M = Nb, Ta) photocatalyst material have been found to be active in water remediation application. The origin of the improved optical absorption of N-doped CsTaWO₆ in the visible region was investigated using PAW method with GGA version of PBE for exchange-correlation effect.^[181] The PDOS analysis revealed that the N 2p and O 2p states at the VBM reduced the band gap by 0.323 eV compared to the pure CsTaWO₆. Moreover, the unfilled N 2p impurity state may act as recombination centers to the charge carriers and enhances the photocatalytic performance. Through B3LYP functional and double-zeta LanL2DZ basis set, the extra electronic states in the Se 3p orbitals influenced the visible light optical absorption performance of Se-doped TiO₂.^[182] Within PAW method, the red-shift absorption of S-doped anatase TiO₂ was attributed to the S 3p impure state above the VB.^[183] In addition, band gap reduction of S-doped TiO₂ was contributed by the increase S concentration via DFT method with PAW

method and PBE of GGA for exchange-correlation effect.^[184] In addition, the electron excitations from the S 3p state to CB may influence the red-shift optical absorption of S-doped TiO₂. Furthermore, the electronic location function analysis revealed ionic character. The band edges of I- and Se-doped β -Ga₂O₃,^[185] and pure graphitic carbon nitride (g-CN), as well as P-doped g-C₃N₄ and g-CN,^[186] were observed to meet the thermodynamic criteria for the overall water splitting compared to the other anions. The origin of the enriched visible light photocatalytic performance of C-doped ZnO was influenced by the extra electron states in the band gap arising from the C dopant via the nonlocal pseudopotentials method of the LDA functional.^[187] A remarkable band gap reduction and enhanced photocatalytic performance of Br-, N-, and I-doped SrTiO₃(001) was observed based on the spin-polarized DFT method with HSE06 hybrid functional and PAW method for the electron–ion interactions.^[188] The enhanced visible light absorption of N-doped SrTiO₃ was attributed to the localized N 2p state found at the VBM.^[189] Based on DFT calculations with GGA functional, the electronic structures of S-doped SrTiO₃ was observed to have raised the energy level of the VBM and induces band gap reduction due to the S 3p state which mixes well with the O 2p state compared to the other doped systems.^[190] In these systems, ultrasoft pseudopotentials and PW91 functional was employed to account for the ionic core and valence electrons interaction.

4.2. Codoping with Metals and Nonmetals

As mentioned previously, doping with either nonmetals or metals has been an effective means to enhance visible light photocatalytic activity of semiconductors. However, metal or nonmetal dopants, having distinct valences, will restrain photocatalytic performance owing to the electron–hole pairs being partially unoccupied impure states acting as recombination centers and the large perturbation at the band edge positions.^[191] Moreover, mono doping may also result in limited solubility due to the spontaneous formation of compensating defects.^[192] The codoping approach involves either nonmetal–metal,^[193] nonmetal–metalloid,^[194] nonmetal–nonmetal,^[195] or metal–metal^[196] pairs resulting in outstanding approaches toward modifying the band structure of semiconductor photocatalyst materials with an improved photoresponse. An ideal codopant should (1) form a charge compensated system to eliminate vacancy defect, (2) easily fit the ionic size into the lattice site of the atoms, and (3) not lower the CBM to a significant extent to keep the semiconductor active. Due to the individual benefits of metal and nonmetal doping, the codopants can combine the two benefits and induce enhanced photocatalytic activity.^[197] For example, The Si–F codoped TiO₂ was thermodynamically more favorable than the Si- and F-doped TiO₂ within GGA of the PBE scheme.^[198] In addition, the enhanced optical absorption of Si–F codoped TiO₂ was because of the decrease in the electron transition energy from the VBM to CBM. The improved visible light absorption performance of C–Mo codoped TiO₂ system have been observed, but the position of the CBM was slightly affected when compared to the pure system.^[199] Through PAW potentials and PW91, band gap

reduction of B–N codoped TiO₂ was influenced by the Fermi-level shift and the midgap states formation.^[200] In addition, band gap reduction of N–P codoped TiO₂ was contributed by the noncompensated effect.^[201] The improved visible light absorption of nitrogen, first row transition metals, such as Sc, Ti, V, Cr, Mn, Fe, Co, Ni, Cu, Zn, and second row transition metal such as, Y, Zr, Nb, and Mo codoped TiO₂ was attributed to the impurity energy state formation in the band gap and the reduced CBM of the codoped systems.^[202] Moreover, band gap reduction, enhanced electron–hole pair separation and lattice distortion in Y–N codoped TiO₂^[203] and N–Eu codoped TiO₂^[204] have been reported. The photocatalytic activity and the improved visible light of C–, B–, and C–B codoped TiO₂ was influenced by the impure states distribution and the location of the Fermi level in the crystal structure created by the dopants through plane-wave pseudopotential approach and GGA of the PBE for the exchange-correlation effect.^[205] The synergistic effect of C–Ag codoped TiO₂ was observed to influence the visible light absorption and band gap reduction.^[206] The enhanced visible light performance of C–N codoped CeO₂ was influenced by the narrowed band gap and strong absorption, which was caused by the impurity states.^[207] The metal (La, V, Y, Ta, Nb, Sc) and nonmetal (I, H, Br, Cl, F) codoping was found to prevent the N-induced discrete states in SrTiO₃ crystal structure through plane wave pseudopotential method and GGA of the PBE scheme.^[208] The La–Rh codoped SrTiO₃ suppressed the formation of photochemically inert Rh⁴⁺ state as well as the formation of a charge-compensated system.^[209] A significant electron cloud overlap of Mo–2N codoped SrTiO₃ was observed and the N electron density was more delocalized toward Mo (Figure 5a).^[210] However, no significant electron cloud overlap was observed in W–2N codoped SrTiO₃ (Figure 5b).

The codoping effect on the photocatalytic performance of NaTaO₃ has been reported with an improved charge carrier mobility due to the continuum band structure formation by the Mo and N codopant.^[211] In addition, the band position of the Mo–N codoped NaTaO₃ was well aligned to satisfy the thermodynamic stability of photooxidation and photoreduction of water. The doping effects of SrTiO₃ on V, Nb, and

Ta with cationic codopant (Na/K/Rh) or anionic codopant (N) was observed to meet the thermodynamic criteria for water splitting with reference to water redox levels.^[212] The synergistic effect on the photoactivity of SrTiO₃ codoped with N and Sb was observed to improve the visible light performance due to the charge compensation.^[213] Moreover, the band position of N–Sb codoped SrTiO₃ are well positioned for the feasibility of H₂ production with respect to the undoped system.^[213] Significant band gap reduction of NaTaO₃ codoped with C–S, N–N, and N–P was observed but can only work as an electrode for water reduction rather than oxidation.

Moreover, the band edge positions of N–N, N–P, and C–S codoped ZrO₂ matched are suitable for the photocatalytic water splitting with improved visible light absorption. The La–Fe codoped NaTaO₃ system was found to be more energetically stable than their corresponding mono doped counterparts.^[214] Moreover, the total density of states showed an unoccupied extra energy state in the band gap and the PDOS analysis produced an intermediate state mainly comprised of O 2p and Fe 3d states located at 1.1 and 2.0 eV above the VBM. The enhanced visible-light response and the band gap narrowing in Mo–N, Cr–N codoped NaNbO₃ have been found to be influenced by the distance and concentration of the codopant.^[215] In addition, the PDOS analysis of Mo-doped NaNbO₃ revealed that the VBM consist of O 2p states and the CBM was controlled by Nb 4d and Mo 4d states. In N–Nd codoped KNbO₃, the VBM was found to compose of O 2p states and the Nb 4d states contributed to the CBM.^[216]

Normally, the optical absorption properties of any semiconductor-based photocatalyst materials, which are associated with its band structure, have been a significant factor influencing the photocatalytic performance. According to Equation (14), the wavelength-dependent absorption coefficients were evaluated by transforming the complex dielectric function to the absorption coefficient (α_{abs})^[217]

$$\alpha_{\text{abs}} = \sqrt{2\omega} \left(\sqrt{\varepsilon_1^2(\omega) + \varepsilon_2^2(\omega)} - \varepsilon_1(\omega) \right)^{\frac{1}{2}} \quad (14)$$

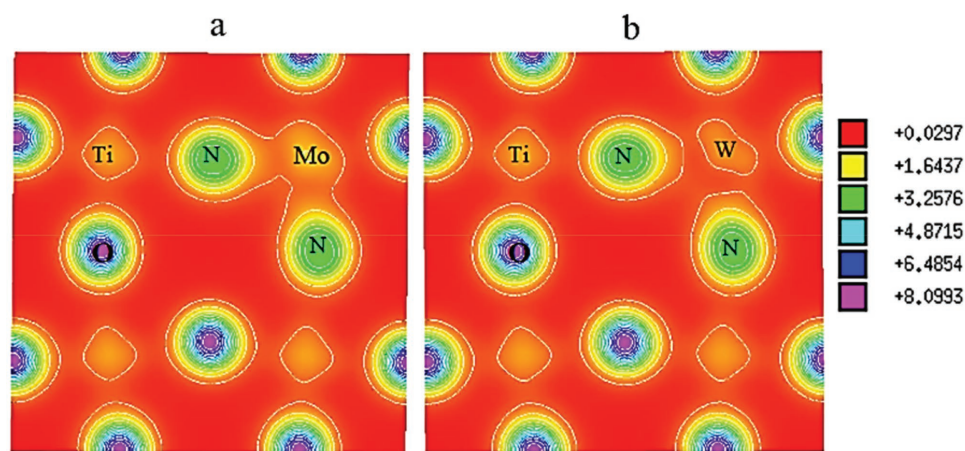


Figure 5. Total charge density distribution for a) (2N, Mo)-codoped SrTiO₃ and b) (2N, W)-codoped SrTiO₃. Adapted with permission.^[210] Copyright 2014, Royal Society of Chemistry.

where $\varepsilon(\omega)$, $\varepsilon_1(\omega)$, and $\varepsilon_2(\omega)$ are the frequency dependent complex, real, and imaginary parts of the dielectric function, respectively. Highly plausible band structure with band gap reduction and enhanced visible-light absorption when KNbO₃ was codoped with N and W have been reported.^[218] In addition, an optical absorption with improved redshift and enhanced photocatalytic activity of anatase TiO₂ codoped with N and Sm have been observed.^[219]

The B–F codoped g-C₃N₄ has been an excellent photocatalyst for O₂ and H₂ generation through water splitting driven reactions in the visible region as opposed to the mono doped systems via HSE06 hybrid functional.^[220] In addition, the band alignments showed that the F-doped and B–F codoped g-C₃N₄ enhanced the oxidation ability, while the B-doped g-C₃N₄ enhanced the reductive ability of g-C₃N₄. The visible light photocatalytic response of W/Mo/W and Mo/W/Mo codoped BiVO₄ was ascribed to the continuum state above the CB edge of BiVO₄, narrow band gap and smaller formation energies via GGA + U of the Dudarev's method.^[221] The BiVO₄ doped with W and Mo enhanced the electron–hole separation without any improvement in the material's optical properties as well as band gap reduction.^[222] Through hybrid HSE06 functional, the electronic properties of F–N codoped Zn₂GeO₄ were investigated.^[223] The redshift visible light performance and the narrow band gap was influenced by the N 2p state formed above the VB edge. Within spin-polarized DFT approach, the ability of compensated codoping to form delocalized states rather than discrete trap levels was found for both H–N and F–N codoped AgTaO₃ without affecting the band edge position desired for the overall photocatalytic water splitting process.^[224]

4.3. Heterostructures

Besides the narrow band gap of any semiconductor-based photocatalysts, a number of charge carriers generated upon light excitation are a significant factor to the photocatalytic performance. The electrons and holes generated upon light excitation should not recombine to enable the occurrence of chemical reactions to enhance the charge separation and the photocatalytic performance. An approach to enrich the separation of charge carriers and extend the optical absorption edge into the visible light region as well as attaining enhanced photocatalytic degradation of contaminants in water/wastewater resources is to combine two or more semiconductors to construct heterojunctions.^[225] The interface between the components of heterojunctions materials plays an important role in tuning the photocatalytic properties and enhanced the visible light performance. The nanostructuring process has been revealed to improve the visible light optical absorption with improved photostability and photoactivity.^[226] Tada et al.^[227] and Libera et al.^[228] were the first to synthesize and deposit FeO_x nanoclusters using chemisorption–calcinations–cycling and atomic layer deposition, respectively. Both methods showed band gap reduction and enriched visible light performance owing to the FeO_x clusters shifting the VBM of titania nanocluster. According to Tian et al.,^[229] ideal heterostructures in photocatalyst should have: (1) enhanced charge separation to form more active radicals; (2) high effective light absorption to make use of the wider portion of the solar energy and (3) large surface area. In heterostructures, the cocatalyst should (1) catalyze the

surface reactions, (2) provide oxidation or reduction active sites, and (3) trap the photogenerated charge carriers to restrain their recombination rate. Hence, it is significant to find a suitable photosensitizer, which can couple with the semiconductor-based photocatalyst to enhanced photocatalytic activity, stability, and selectivity. Recently, several heterostructures such as TiO₂/Bi₂WO₆,^[230] CuS/ZnO,^[231] Cu₂O/SrTiO₃,^[232] TiO₂/ZnO,^[233] MoS₂/SrTiO₃,^[234] SrTiO₃/TiO₂,^[235] CdS/Ta₂O₅,^[236] Bi₂O₂CO₃/Bi₂MoO₆,^[237] BiOBr/ZnFe₂O₄,^[238] BiVO₄/WO₃,^[239] Bi₄Ti₃O₁₂/TiO₂,^[240] SnO_x/ZnGa₂O₄,^[241] and others have been found to exhibit enhanced visible-light absorption with improved photoactivity. Considering these experimental findings, it is significant to know the underlying origin of the enhanced visible light performance of these hybrid nanocomposites. Without fully understanding of these fundamental electronic structures, it is difficult to optimize and enhance the photocatalytic activity. Recently, first-principles prediction on heterostructures photocatalysis has emerged as a new discipline in science and technology. First-principles calculation allows the fundamental understanding of material and process, interprets experimental data from diverse experimental techniques, and opens exciting possibilities to design novel material. First-principles calculations on heterostructures that contain relevant interface of the constituent materials are used to study interface effects. For example, the interfacial properties of WO₃/BiOCl heterojunction were explored through DFT study with PAW method and PBE of the GGA functional for exchange–correlation effects.^[242] The atoms of the interface models were relaxed and the interface distance optimized with conjugate gradient approach. The PDOS analysis revealed a suitable band alignment induced by the interfacial structures with enhanced separation of the excited carriers to reduce the recombination rate of the photogenerated charge carriers. The absence of interfacial gap states influences the charge migration from the VBM of BiOCl to the CBM of WO₃. Moreover, the optical absorption response of WO₃/BiOCl heterojunction was observed to shift to a longer wavelength region compared to the bulk BiOCl (Figure 6).

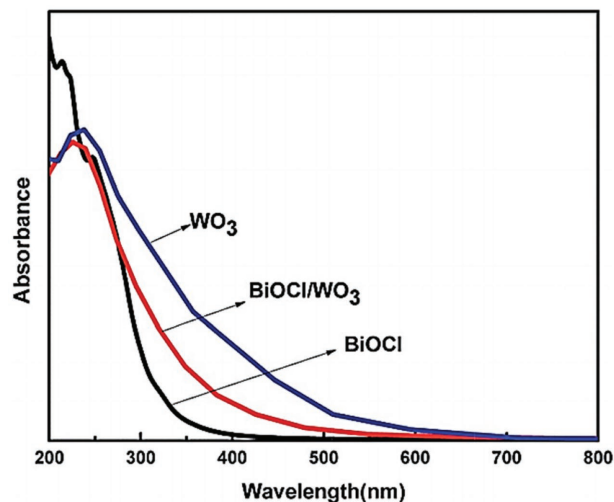


Figure 6. Optical absorption spectra of BiOCl, WO₃, and WO₃/BiOCl heterojunction. Adapted with permission.^[242] Copyright 2014, Royal Society of Chemistry.

Although there is no previous experimental study on Ga₂O₃-modified TiO₂, there have been some studies on MgO-modified TiO₂.^[243] First-principles study of these heterostructures confirms previous experimental results. Band gap reduction and enhanced separation of charge carrier with improved photocatalytic activity after light excitation were observed when MgO/Ga₂O₃ was modified with TiO₂ through DFT + U method with Blöchl's PAW approximation for the core–valence interaction and the PW91 functional for the exchange–correlation effect.^[244] In this system a U parameter was applied to the Ti 3d state, as well as the O 2p state because the traditional DFT approach cannot effectively account for the localized oxygen hole states.^[245] For instance, the excited state of MgO(Ga₂O₃)/TiO₂ heterostructures reveal that upon light excitation, the electron–hole pairs were able to be separated onto the TiO₂ surface, thereby reducing the charge recombination and enhance its photocatalytic performance. Through plane wave basis set and PW91 for the exchange–correlation functional, incorporation of Bi₂O₃ nanoclusters into rutile TiO₂(110) crystal structure resulted in band gap narrowing owing to the upward shift of the VB edge.^[246] Based on the electron–hole localization analysis, the photoexcited states demonstrate improved charge separation when Bi₂O₃ was coupled with monolayer rutile TiO₂(110) surface. Within DFT + U method, the origin of the improved photoactivity of TiO₂ modified with iron oxide species (FeO, FeO₂, and Fe₂O₃) was contributed by the charge separation at the TiO₂ surface.^[247] The Blöchl's PAW method and PW91 approximation was employed to account for the core–valence interaction. In addition, the PEDOS analysis reveal that the iron oxide clusters adsorbed at the TiO₂(001) surface was stable and lied above the VB to narrow the band gap toward the visible light region. Furthermore, the excess spin density showed an excess spin electron on each Fe in the adsorbed FeO_x (x = 1, 2, 3) with no unpaired electrons on the Ti surface.^[247] A significant charge separation of the charge carriers onto the surface of the anatase TiO₂ and the Sn(II)O nanocluster was observed.^[248] In addition, the spin density showed a localized hole on the two Sn–O bonds.

Through DFT + U approach with PAW potentials for the core–valence interaction and PW91 functional for the exchange–correlation, the enhanced photoactivity of rutile TiO₂ modified with ZnX (X = O, S, Se) nanocluster was attributed not only to the localized holes and electrons on the TiO₂ surface but also to the low coordinated anion site on the adsorbed ZnX nanoclusters.^[249] The nature of the CB and VB edges, as well as the band gap reduction, were controlled by the oxidation state of Pb in the supported PbO nanocluster based on DFT + U approach with a U value of 4.5 eV for Ti 3d state and PAW potentials for the core–valence interaction.^[250] Within DFT + U approach and PW91 approximation, the enhanced visible light absorption and band gap reduction of TiO₂ nanocluster modified rutile TiO₂ were ascribed to the new nanocluster derived states formed at VBM edge.^[251] The PDOS analysis revealed an upward VB shift and narrow band gap, owing to the formation of derived state, while the CB remain unchanged with contribution from Ti 3d state. The band alignment significantly favored the separation of the electron–hole pairs after light excitation with enhanced photocatalytic activity of the nanocomposite.

Currently, noncovalent forces, such as van der Waals interaction and hydrogen bonding are essential to the formation and stability of photocatalyst materials. However, this long-range interaction cannot be accounted properly by the most sophisticated gradient-corrected XC, local-density the functionals of DFT and the HF wave function. Recently, several hybrid semiempirical approaches have been developed to introduce damped atom-pairwise dispersion correction of the form C₆R⁻⁶ to the DFT method. These methods offer the best compromise between the necessity to enhance nonbonding interaction and the cost of calculation of the dispersion terms. A comprehensive study has shown that the combination of semiempirical with DFT method and pairwise corrections offers a dramatic enhancement compared to the traditional DFT methods in terms of energy calculation and structure description. This approach has been established to evaluate the role of long-range dispersion interactions at the interface of semiconductor-based heterojunction materials. For instance, the carrier separation, as well as the restrained recombination of e⁻/h⁺ pairs in g-C₃N₄/CdS(110) interface, was found to be influenced by the internal electric field using HSE06 hybrid functional with PAW and PBE-D2 method for long-range van der Waals interaction due to the presence of weak bonding interaction between CdS and g-C₃N₄.^[252] In addition, g-C₃N₄/CdS heterojunction exhibited higher quantum efficiency under simulated visible light irradiation than the individual g-C₃N₄ and CdS. As shown in **Figure 7**, the lower work function of g-C₃N₄ indicated electrons might flow from g-C₃N₄ to CdS. Hence, g-C₃N₄ may be positively charged, while CdS may be negatively charged near the interface owing to electrostatic induction.

Due to the pinning of the Fermi level at the energetic position of charged surface states, a built-in electric field directed from g-C₃N₄ to CdS occurred to reduce the electron–hole recombination. Moreover, the built-in electric field at the interface enhances the separation and migration of the photogenerated electron–hole pairs, thereby enhancing the photocatalytic performance of the nanocomposite. The built-in electric field refers to the interfacial electric dipole field generated by the electron–hole separation at the semiconductor heterostructures. A photocatalyst material with a built-in electric field at the semiconductor interface might be an ideal redox mediator-free system. The built-in electric field below the semiconductor surface is one of the main driving force for charge separation during photocatalysis process.^[253] In the space charge region, the band edges potential may be shifted continuously due to the built-in electric field at the junction.^[254] Therefore, the excitation of photogenerated electrons and holes across the interface can participate in the redox reaction.^[255]

To characterize the various band alignments that normally occurred in nanocomposites, three types of heterojunction were considered as shown in **Figure 8**.

A Type-I heterojunction occurs when the CB and VB of component B is at a lower and higher energy than component A. Hence, electrons and holes will be transferred and accumulate on component A. In addition, a type-II heterojunction occurs when the photoexcited electrons are transferred from component B to component A owing the higher negative potential of B compared to A. The photoinduced holes can be transferred in the opposite direction to the enhanced the charge separation

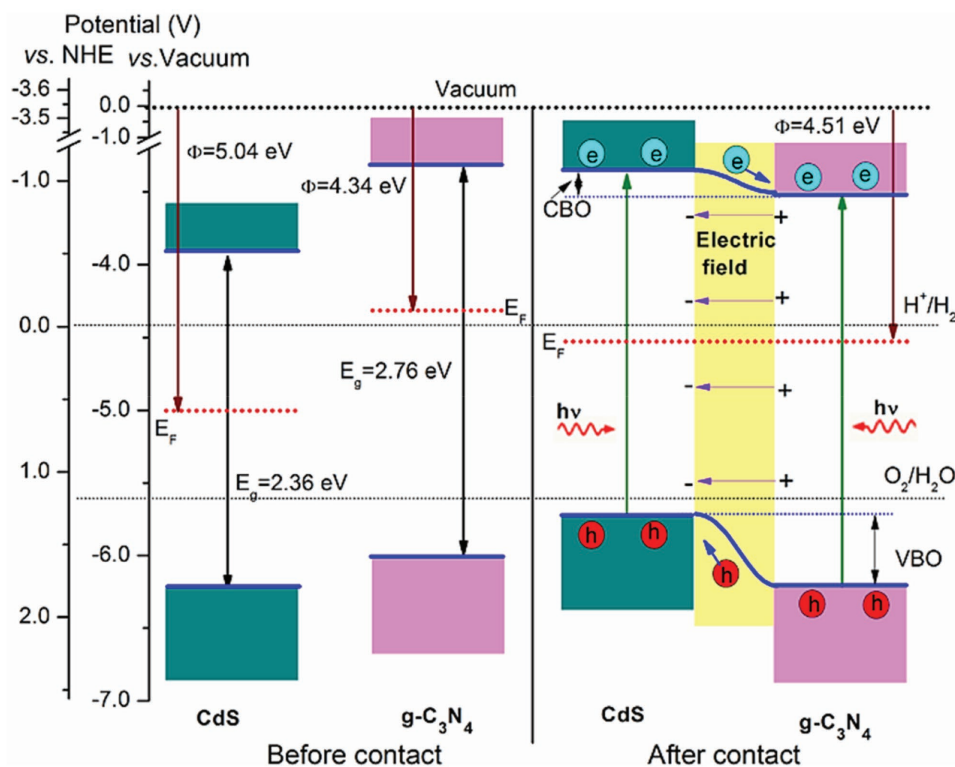


Figure 7. Band edge positions before and after contact of $g\text{-C}_3\text{N}_4$ and CdS where CBO, VBO, E_g , and E_f represent the CB offset, VB offset, band gap, and Fermi energy level, respectively. Adapted with permission.^[252] Copyright 2015, Royal Society of Chemistry.

and the photocatalytic performance. Type-III heterojunction is similar to the Type-II heterojunction but the most prominent difference in the CB and VB edges, which offers a higher driving force to the charge transfer.^[256]

The energetic, optical and electronic properties of a $g\text{-C}_3\text{N}_4(001)/\text{BiVO}_4(010)$ nanocomposites has been explored using GGA + U method with PAW approach for the core-valence interaction and GGA of the PBE for the exchange-correlation effect.^[257] In addition, the DFT-D3 method^[258] with Becke and Johnson-damped^[259] van der Waals correction proposed by Grimme was adopted since weak bonding interactions were expected to play an essential role in this nanocomposite. The $g\text{-C}_3\text{N}_4/\text{BiVO}_4(010)$ nanocomposite exhibited a favorable type-II band alignment to enhance the separation of the photogenerated charge carriers and restrain the recombination rate, thereby improving the photocatalytic performance of the nanocomposite.

Moreover, the charged interface of the $g\text{-C}_3\text{N}_4/\text{BiVO}_4(010)$ nanocomposite was comparable to the space charge region of the novel $g\text{-C}_3\text{N}_4/\text{MoS}_2$ nanocomposite.^[260] Based on HSE06 hybrid functional with GGA of PBE form and van der Waals correction proposed by Grimme, the calculated band alignment between MoS_2 sheets and $g\text{-C}_3\text{N}_4$ monolayer showed an increase of 0.15 and 0.83 eV by the VBM and CBM, respectively of the $g\text{-C}_3\text{N}_4$ monolayer compared to the MoS_2 sheet. The frozen-core PAW method was used to account for the core-valence electrons effects. The predicted type-II band alignment allows the effective transfer of the photogenerated electrons from the monolayer $g\text{-C}_3\text{N}_4$ to the MoS_2 sheet (Figure 9).

This charge transfer results in a polarized field within the interface region to enhance the separation of the photogenerated charge carriers and the redshift absorption of the hybrid layered nanocomposite.

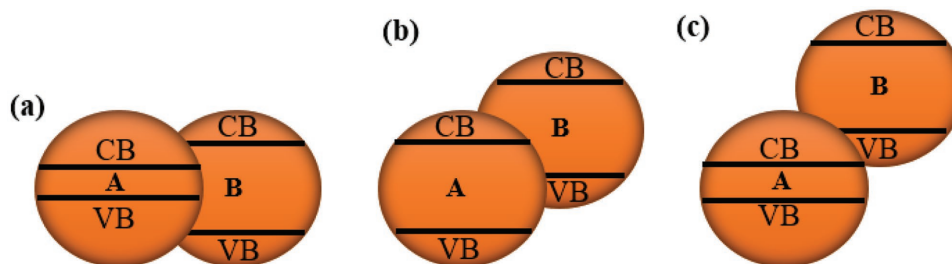


Figure 8. The various types of heterojunctions. a) Type I, b) type II, and c) type III, where A and B correspond to semiconductor A and B, respectively.

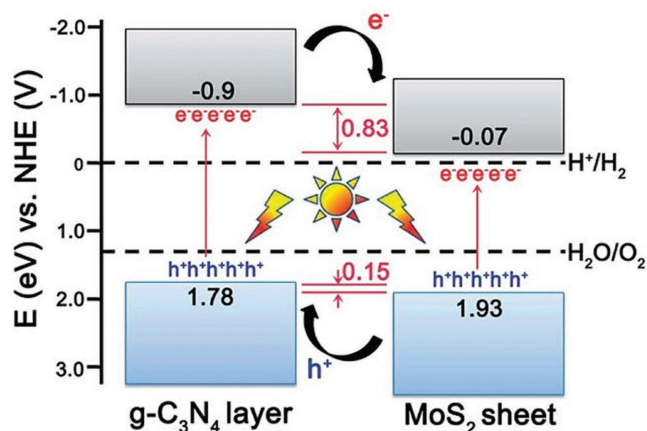


Figure 9. Illustration of the transfer of the photogenerated charge carriers in the g-C₃N₄/MoS₂ nanocomposite. Adapted with permission.^[260] Copyright 2014, Royal Society of Chemistry.

The electronic structure and optical property of WS₂/MoS₂ composite were studied and the composite exhibited a staggered type-II band alignment due to the photoexcited electrons migration from the VB of WS₂ into the CB of MoS₂.^[261] The proper charge distribution at the interface facilitated the separation of charge carriers to restrain the photogenerated electron-hole pairs recombination.

4.4. Nanocarbon-Based Composite

Carbon has been established to create apparent solid-state allotropes with various properties and structures ranging from sp³-hybridized diamond to sp²-hybridized graphite.^[262] Carbon nanomaterials, are consisted to be comprised of solely sp² bonded graphitic carbon, which is observed in all reduced dimensionalities, such as fullerene, graphene derivatives, and carbon nanotubes (CNTs). CNTs, graphene derivatives, and fullerene have recently been used to interface with semiconductor-based photocatalysts to enhance their visible-light activity compared to the bulk semiconductors.^[263] The improved photocatalytic activity of carbon/semiconductor nanocomposites is normally attributed to the electron-accepting, as well as the transport properties of carbon nanomaterials due to their ability to provide a conducive route to direct the migration of the photogenerated charge carriers.^[264] In addition, their uncommon chemical and physical properties have influenced a comprehensive investigation on carbon nanomaterials owing to their great promising applications.^[265]

4.4.1. Carbon Nanotube

Carbon nanotubes arose into the scientific spotlight in 1991,^[266] and since then CNTs have been a focal point of several studies. As a metal-free cocatalyst, CNT materials exhibited strong potential to enhance the activity of the photocatalytic H₂-production^[267] and degradation of pollutants^[268] owing to their large specific area (>150 m² g⁻¹), as well as outstanding mechanical and electronic properties.^[269] The synergetic effect and

enhanced photocatalytic performance of CNTs/semiconductor materials, where CNTs act as an electron sink to decrease the recombination of the of charge carriers as well as a photosensitizer to generate electrons and holes have been observed.^[270] For example, enhanced visible-light absorption of Ag-doped and pure ZnO single-walled CNTs have been observed using GGA + U approaches with double numerical plus d-functions basis set and effective core potentials.^[271] In addition, the enhanced absorption intensity of Ag-doped ZnO nanotubes was attributed to the increase concentration of Ag. Efficient charge separation and visible-light photoactivity across the interface of CNT/TiO₂ hybrid materials compared to the metallic CNT/TiO₂ system have been reported based on DFT + U method with PBE parametrization of the GGA.^[272] The onsite U and J value of 6.0 and 0.5 eV, respectively, were used for the Ti 3d states. By contrast, a significant charge transfer from the metallic CNT to the TiO₂ was observed due to the strong interaction between them, which later decreases the built-in potential and the charge separation. The CNTs introduced onto the TiO₂ surface contributed to the reduced recombination of the photogenerated charge carriers as well as the enhanced photocatalytic performance of TiO₂/CNT nanocomposite under simulated visible light irradiation based on the framework of DFT as implemented in Dmol³ package with PBE parametrization of GGA for the exchange-correlation potential.^[273] Ultrasoft pseudopotential was used to treat the electron-core interaction of all the atoms within the nanocomposite.

4.4.2. Fullerenes

Fullerenes (C₆₀) serve as another allotrope of C with a special electronic property. Here, C₆₀, C₂₆, and C₂₀ are considered as the typical fullerenes, inspired by their unique properties and structures.^[274] The C₆₀ with a closed-shell configuration comprising of 30 bonding molecular orbitals with 60 π-electrons induce effective electron transfer.^[275] The unusual structure of C₆₀ serve as an outstanding electron acceptor to effectively enhance the photoinduced charge separation.^[276] C₂₀ which consists mainly of pentagons is the smallest among the fullerene forms,^[277] while fullerene C₂₆ is an intermediate and pure open-shell compound.^[278]

Fullerenes are known as single oxygen sensitizers to the electron acceptor-donor and have been used in photocatalysis.^[279] In photocatalytic systems, fullerene can create a space potential difference to enrich the separation and migration of the photogenerated charge carriers, as well as tuning the band gap.^[280] The amount of charge transfer in WS₂/fullerenes^[281] and MoS₂/fullerene (C₆₀, C₂₆, and C₂₀)^[280] heterostructures was found to depend on the nature of the fullerene. In addition, a type-II staggered band alignment, which was formed in the MoS₂/C₂₀ and WS₂/fullerenes heterostructures, contributed to the enriched photocatalytic performance and the reduced charge recombination. Fullerene modification was found to be a useful approach to enhance the photoactivity of Ag₃PO₄ via plane wave DFT/LDA + U approach implemented in CASTEP code.^[282] The U parameters of 7.2, 7.0, and 7.0 eV was used for the Ag 4d, O 2p, and P 3p states, respectively. The nanocomposites showed band gap reduction, improve

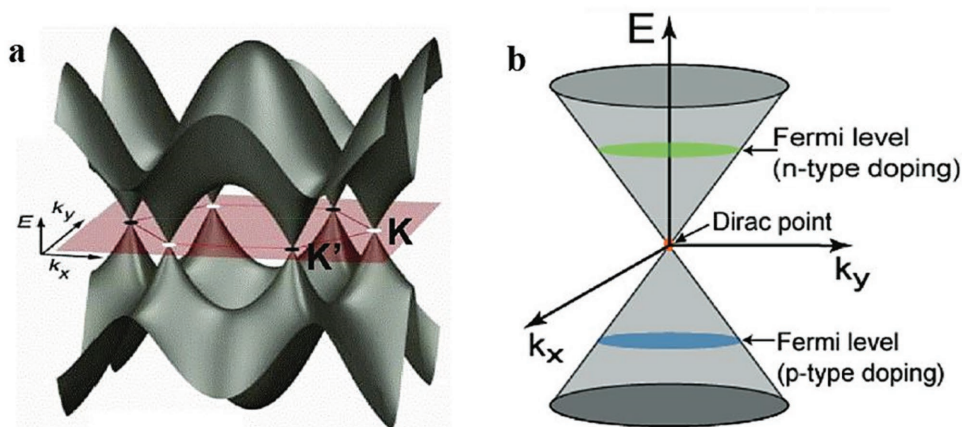


Figure 10. a) Graphene band structure and b) Fermi level position. Reproduced with permission.^[287] Copyright 2010, American Chemical Society.

photoinduced electrons transfer and visible light optical absorption compared to the pure Ag_3PO_4 . In addition, a type-II staggered band alignment was obtained at the interface of $\text{C}_{26}/\text{Ag}_3\text{PO}_4$ nanocomposite, which effectively reduced the charge recombination to enhance the photocatalytic performance. Enhanced photocatalytic activity of anatase TiO_2 by fullerene modification was studied within PAW method and GGA functional of the PW91.^[283] The improved charge separation and visible light absorption of $\text{C}_{60}/\text{TiO}_2$ surface contributed not only to the band gap narrowing but also the formation of additional states between the VB and CB. In all these nanocomposites, the role of fullerene was (1) to act as space potential difference and sensitizer to enhance the separation of the photogenerated charge carriers, and (2) to tune the band structure of the nanocomposites by narrowing their band gap. These results revealed narrowed band gap of the nanocomposites when the semiconductor-based photocatalysts were incorporated with fullerene, which subsequently enhanced their visible light absorption and photocatalytic performance. In addition, the electrostatic potential distributions at the interface with the potential of the nanocomposites higher than that of the fullerene could significantly decrease the recombination of charge carriers and enhanced the photocatalytic performance. These studies offer an in-depth knowledge into optimizing the photocatalytic properties of fullerene-based photocatalyst materials.

4.4.3. Graphene

Graphene (GR), with a 2D hexagonal structure of sp^2 hybridized C atoms, exhibits remarkable properties, such as high thermal conductivity (≈ 2000 to 5000 W m K^{-1}), fast mobility of charge carriers ($\approx 100\,000 \text{ cm}^2 \text{ V}^{-1} \text{ s}^{-1}$), large theoretical specific expose area ($\approx 2630 \text{ m}^2 \text{ g}^{-1}$), superior mechanical strength ($2.4 \pm 0.4 \text{ TPa}$), good optical transparency, and ability of sustaining large electrical current density (108 A cm^{-2}).^[284] All these properties make graphene a viable cocatalyst to accept electrons for exciton separation. Graphene, being a fascinating material has potential applications in water treatment.^[285]

An ideal graphene sheet is considered as an infinitely large aromatic molecule devoid of C vacancies.^[286] The C atoms form

three strong C–C bonds with the three adjacent C atoms, while the remaining π -orbital overlaps to produce a π^* -state CB and a π -state VB. The VBM and CBM of graphene meet at the K and K' points (Fermi level), which is positioned at the corners of the honeycomb Brillouin zone as shown in Figure 10a.^[287]

The VB and CB of graphene at the Brillouin zone corners makes a graphene sheet a zero band gap semiconductor.^[288] The close carbon–carbon distance leads to intensive overlapping of electronic bands with the electrons and holes in graphene behaving similarly to mass-free charges.^[289] Tuning the electronic properties of graphene by introducing heteroatoms or functionalities extends the applications of graphene to photocatalysis processes.^[290] Doping graphene with several groups of functionalities can induce an n- or p-doped conductivity based on the nature of the Fermi level shifted by the dopant (Figure 10). Under simulated sunlight irradiation, the generated electrons of GR/semiconductor nanocomposites are captured by GR and simultaneously migrated to the GR surface, which eventually restrain the recombination rate of the charge carriers. As a result, graphene-based semiconductor nanocomposites has abundantly been applied in the photodegradation of pollutants.^[291] Since graphene was discovered in 1986,^[292] several graphene composites with semiconductors, such as TiO_2 ,^[293] MoSe_2 ,^[294] ZnO ,^[295] Ag_3PO_4 ,^[296] MoS_2 ,^[297] SnO_2 ,^[298] and others have been reported as excellent photocatalyst materials. In order to comprehend the influence of interface structure on the semiconductor properties of graphene, the interface of graphene on ZnO slabs and layers were reported via double numeric quality basis set and semicore pseudopotentials approach with GGA functional of PBE for exchange–correlation effect.^[299] Weak interactions between graphene sheet and ZnO layers was found. However, the thick ZnO slabs with polarized surfaces showed stronger binding energies and larger charge transfers. The synergistic effect of $\text{TiO}_2/\text{graphene}/\text{MoS}_2$ ternary nanocomposites was explored via conjugated gradient minimization technique with double zeta plus polarization basis sets and norm-conserving pseudopotential.^[300] The enhanced electron–hole separation in the TiO_2 clusters was due to the accumulation of the excited electron in the MoS_2 film and graphene. Through plane-wave method and ultrasoft pseudopotential, graphene with epoxy interaction with TiO_2 cluster exhibited high binding

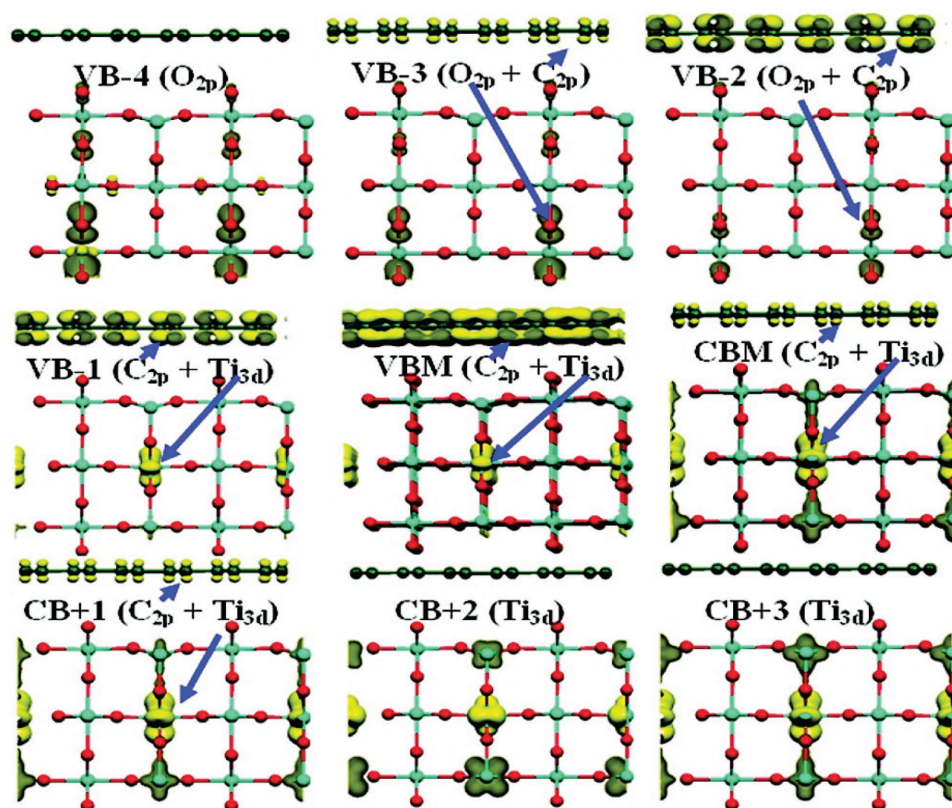


Figure 11. Electron and hole density plot distributions for the CB and VB states. Adapted with permission.^[303b] Copyright 2011, American Chemical Society.

energy and stronger electron cloud overlaps compared to pristine graphene and graphene with monovacancy models.^[301] Through LDA method with plane wave basis set and norm conserving pseudopotential, the enhanced visible light absorption of TiO₂(001)/graphene nanocomposite was contributed by the graphene hybridization.^[302] For instance, the TiO₂-epoxy graphene nanocomposite showed the lowest excitation energy and the highest binding energy compared to the other nanocomposites due to its zero band gap. The PDOS and energy bands results offer significant information on the photocatalytic mechanism relating to the electron excitations from the O 2p state to the C 2p of the nanocomposites. The enhanced charge transfer from graphene to rutile TiO₂^[303] and ZnO^[304] was attributed to the large work function difference at the interface. Moreover, electrons in VBM, VB-1, VB-2, and VB-3 are excited into the surface of Ti 3d states under visible-light irradiation (Figure 11).^[303b]

The enhanced charge transfer and visible light absorption of graphene/anatase TiO₂ (G/ATN)^[305] and graphene/Bi₂WO₆(010)^[306] nanocomposites was attributed to the difference in their work functions within first-principles DFT calculation. The Bader charge and charge distribution analysis revealed a strong covalent bonding between graphene and monolayer Bi₂WO₆(010) surface, which induces a narrow band gap. In addition, both G/ATN and graphene/Bi₂WO₆(010) exhibited high visible light photocatalytic performance compared to the pure TiO₂ and Bi₂WO₆ facets, respectively.

Through LDA and DFT-D2 method proposed by Grimme, the interfacial interaction between graphene and SrTiO₃,^[307] ZnO,^[304]

and Ag₃PO₄^[308] nanocomposites were due to van der Waal interactions rather than covalent forces. Fe-doped TiO₂/graphene nanocomposites were reported to show higher stability than TiO₂/GR nanocomposites owing to the higher charge transfer from the doped semiconductor to the GR sheets.^[309] Structural and molecular adsorption of TiO₂ adsorbents on functionalized graphene and pure graphene nanoribbons were also investigated within GGA functional of PW91 and PAW scheme.^[310] A significant physical adsorption of TiO₂ nanostructures on all the chemical adsorption sites of functionalized graphene nanoribbons, as well as graphene sheets, was found. Through GGA of Perdew–Wang99 functional and semicore pseudopots method, the electronic properties and chemical structure of titania/graphdiyne (GD) and titania/graphene (GR) nanocomposites with different titania facets were studied.^[311] Superior charge separation and oxidation properties of TiO₂(001)-GD composite compared with the pure TiO₂(001)-GR and TiO₂(001) composite was established via HSE06 hybrid functional and PAW method. The charge redistribution at the interface of GR/g-C₃N₄ nanocomposites led to strong electron accumulation below the g-C₃N₄ monolayer and electron depletion above the GR sheet to enhanced the separation of H₂O reduction and oxidation reactions.^[312]

4.4.4. Graphene Oxide and Reduced Graphene Oxide

Graphene oxide (GO) is a GR sheet with epoxy and hydroxyl groups on the basal plane as well as quinone, carboxyl,

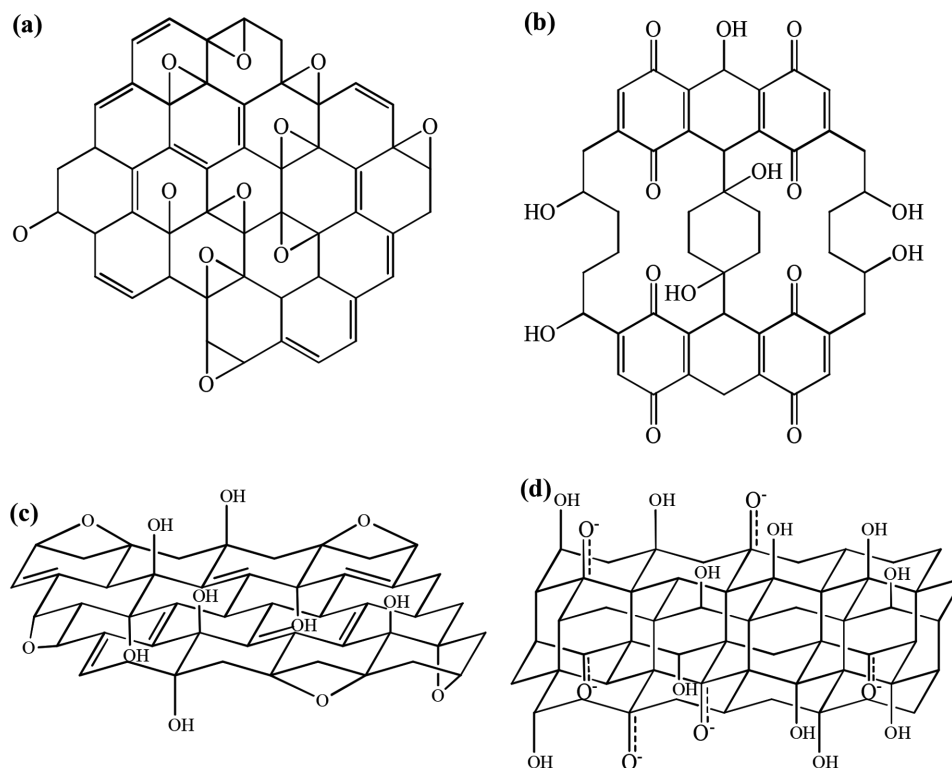


Figure 12. Structural models of GO proposed by a) Hofmann, b) Scholz–Boehm, c) Ruess, and d) Nakajima–Matsuo. Adapted with permission.^[319] Copyright 2006, American Chemical Society.

lactone, phenol, and carbonyl at the sheet edges.^[313] The polar oxygen functional groups make GO negatively charged and hydrophilic in many solvents, especially in water.^[314] Chemical treatment or thermal annealing can remove the functional groups on graphene oxide to form reduced graphene oxide (rGO).^[315] rGO is an excellent adsorbent toward aromatic pollutants compared to GO sheet due to its excellent hydrophobicity, lower oxygen content, and large surface area.^[316] rGO with a superior electrical conductivity and enhance carrier charge mobility proved as good media for electron transfer.^[317] GO has been synthesized using Hummers' method.^[318] Formerly, graphene oxide model was formed as a regular and periodic lattice structure. As at now, several structures of graphene oxide have been proposed.^[319] The Hofmann model involves epoxy groups which span over the basal plane with a general formula of C_2O (Figure 12a).^[320] Ruess^[321] later modified the Hofmann model by including hydroxyl groups to replace the hydrogen atoms of GO (Figure 12b). The epoxide groups were removed in the Scholz–Boehm model (Figure 12c).^[322] The Nakajima and Matsuo model^[323] was based on the theory of a lattice framework to create a stage 2 graphite intercalation compounds (GICs) (Figure 12d). GICs are complex materials having a CX_m formula, where the X^{n-} or X^{n+} ions are inserted between the oppositely charged carbon layers.^[324]

In 1998, Lerf et al.^[325] established a nonperiodic model (Figure 13), which consisted of hydroxyl and epoxy groups attached to the basal plane, with carboxyl and carbonyl groups attached to the edges.

The Lerf–Klinowski model^[326] is nonstoichiometric and mostly amorphous owing to distortion from the high fraction of the sp^3 C–O bond. This model has become the most extensively used model.^[327] GO and rGO, having a tunable band gap (2.4–4.3 eV), large specific surface area, and the presence of several polar functional groups at the surface are extremely suitable 2D nanosheets.^[328] GO alone can be used as a next-generation photocatalyst because of its tunable electronic properties, depending on its applications.^[329] The VB and CB of GO/rGO involve antibonding π -orbitals (π^* -orbitals) of carbon atoms and 2π -bonding of oxygen. Concurrently, nanocomposites of GO and rGO, such as ZnS/rGO,^[330] ZnO/rGO,^[331] Ag_3PO_4 /GO,^[332] Cu_2O /rGO,^[333] MoS_2 /rGO,^[334] SnS_2 /GO,^[335] TiO_2 /rGO,^[336] ZnO/GO,^[337] CuS /GO,^[338] $ZnIn_2S_4$ /rGO,^[339] and others have been shown to be high-performance photocatalysts. The search for efficient visible light harvesting systems has motivated several researchers to design GO(or rGO)-based semiconductor nanocomposites for photocatalysis application. However, the major issue of GO(or rGO)-based nanocomposites is to understand the interfacial interaction between the individual components in the nanocomposites. This challenge remains unclear after extreme experimental study. First-principles study has been the most promising tool to address the interfacial interaction, which is a contributing factor to photocatalysis. The electronic structure and interfacial charge transfer in hybrid CeO_2 /GR(rGO) nanocomposites have been investigated within DFT/LDA + U method with PAW approach.^[340] LDA functional implemented was due to the long-range van der Waals interaction, which was anticipated to be significant in this system.

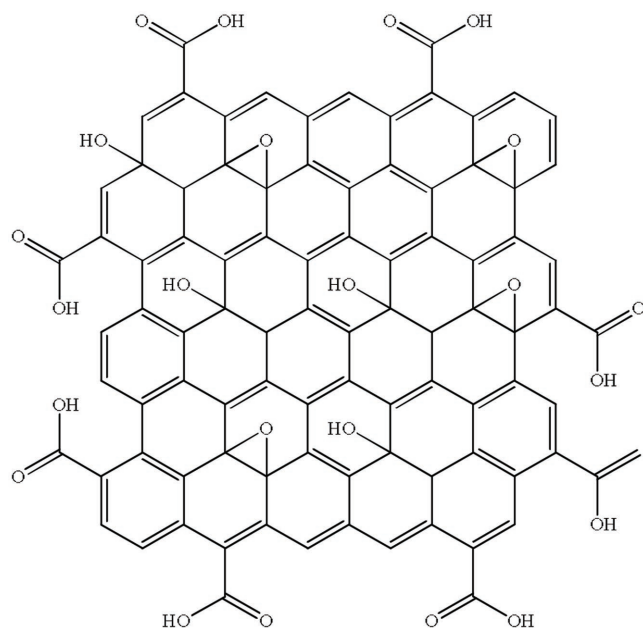


Figure 13. The Lerf-Klinowski model.^[325]

The interfacial interaction of CeO₂/rGO was found to be much stronger than that of CeO₂/GR due to effective charge separation across the CeO₂/rGO interface. In the addition, the interfacial interaction was able to tune the band structure of the nanocomposites, making the CeO₂(111)/GR nanocomposite a type-I band alignment, and the CeO₂(111)/rGO nanocomposite a staggered type-II band alignment. Furthermore, the negatively charged O atoms on the rGO surface act as active sites to narrow band gap and improved the photocatalytic activity of CeO₂(111)/rGO nanocomposite compared to the CeO₂(111)/GR nanocomposite and the pure CeO₂ nanocluster. The PBE of GGA with weak van der Waals correction based on Grimme's scheme^[341] was used to gain an in-depth knowledge of the improved visible light photocatalytic performance of the g-C₃N₄/rGO nanocomposites.^[342] The optical absorption spectra of g-C₃N₄/rGO nanocomposites exhibited enhanced photocatalytic performance due to the negatively charged oxygen atoms on the rGO surface, which was acting as active sites. The interaction at the interface was able to alter the band structures with a type-I heterojunction existing between the g-C₃N₄/rGO nanocomposite with a lower concentration of O atoms, while a staggered type-II band alignment exists between the g-C₃N₄/rGO nanocomposite with a higher concentration of O atoms.

4.5. Challenges of First-Principles Calculations

Electronic structure studies on metals are capable of attaining accurate results and the limitations mostly center on the inclusion of entropy effects. For insulators and semiconductors, achieving such accuracies has been difficult owing to the approximations in the electron-correlation functionals, especially when comparing with experimental studies on charge transition. A large number of parameters, such as sampling of the Brillouin zone, the choice of basis set and supercell size are required in electronic

structure calculations of any semiconductor-based photocatalyst materials. Although these parameters can be controlled because they can be gradually enhanced until convergence is achieved. However, sometimes the available computational resources limit the extent to which this convergence (supercell-size convergence) can be reached. Apart from the issue regarding the supercell size, an effective *k*-points sampling of the Brillouin-zone of electronic structure calculation is also significant. The Brillouin-zone integrations are obtained by replacing the integrals with a set of special points to offer a precise approximation of the integrated quantity and preserve the symmetry of the system. In principle, the Brillouin-zone integrations are generated by the Monkhorst-Pack scheme^[343] as a spaced mesh of $m \times m \times m$ *k*-points in the *k*-space of the unit cell. Normally high symmetry points, such as Γ point need to be prevented to avoid the enclosure of local minima or maxima into the band structure. Consequently, odd values of "*m*" are utilized when Γ point is excluded from the Brillouin-zone sampling. The required size of "*m*" is based on the physical quantity of the material under consideration and metals normally require extensively large *k*-point sets compared to semiconductors.

5. Conclusion and Outlook

Recently, semiconductor-based photocatalysts have received much attention, with TiO₂ dominating as an essential material in the environmental remediation application. However, intrinsically most of these semiconductors are unable to show photocatalytic activity in the visible region due to their wide band gap. Moreover, high recombination rate is also another critical factor that reduces the solar energy conversion efficiency. Up to now, a wide-range of metal sulfides, oxides, and nitrides have been successfully designed for applications in the photodegradation of pollutants and water splitting. In this review, we have extensively covered the fundamentals and underlying mechanism of the enhanced optical absorption and photoactivity of semiconductor-based photocatalyst materials. For instance, band gap reduction and band alignments relative to the redox potential of water have also been reviewed in detail to account for the change in the photocatalytic performance. Moreover, the state-of-the-art first-principles calculation of semiconductor-based photocatalyst materials was considered. We have also discussed how improvement in DFT extremely addressed the band gap issue with reference to the traditional GGA and LDA functionals, which have been used in photocatalysis for several years. First-principles calculations also offer an in-depth knowledge into several physical properties, which are not accessible via experimental studies. Moreover, the reliability and accuracy of modern first-principles calculations are comparable to several experimental studies.

Although considerable progress about the understanding of the optical and electronic properties of semiconductor photocatalysis has received much attention, research in this field is still at the fundamental stage and further improvements are needed. Understanding the charge transport mechanism in photocatalytic water splitting is essential to the reaction rate since the reaction is thermodynamically uphill and relies on the effective transfer of energetic charges. In addition, the control understanding of charge separation and transport in

multicomponent heterostructures have been progressively more difficult, since the interface properties of semiconductor photocatalyst materials determine the photocatalytic performance. In addition, the mechanisms behind the overall photocatalytic enhancement of the semiconductor nanocomposites systems partially remain unexplained. Previous studies have demonstrated the advantages of carbon materials in facilitating water splitting, whereas the underlying charge transport mechanism for the illuminated carbon-based nanocomposites still remain controversial. With this understanding, the fundamental studies on the origin and underlying mechanism of visible light responsive photocatalysts, charge transfer and separation at the interface may be explored. The interfacial contact and bonding between carbon nanomaterials and semiconductors in nanocomposites also need clarification. In literature, the improved photocatalytic activity has also been attributed to the synergistic effects induced by the interfacial interactions of semiconductors with carbon nanomaterials or other semiconductors. Knowing the detailed electronic properties and the interfacial electron transfer process will aid the design and fabrication of best materials for photocatalytic water splitting.

The design of first-principles approaches and software packages allow experimentalists to fabricate existing and new materials. However, the major challenges involve the incorporation of first-principles calculations, databases, and atomistic modeling into a single system, so that the realization of efficient design of hybrid materials, as well as visualizing their synthesis reactions can be achieved. Currently, the hybrid functionals, which provide accurate results in electronic structures, cannot clearly provide a universal solution to the long-range van der Waals interaction. Thus, new functionals, which can precisely address both the electron correlation effect and van der Waals interactions, are significant.

Acknowledgements

The authors would like to acknowledge the financial contributions from the Faculty of Science: University of Johannesburg-South Africa, Center for Nanomaterials and Science Research: Department of Applied Chemistry and the National Research Foundation (TTK14052167682). The financial support from the Global Excellence and Stature (GES) Doctoral Scholarship: University of Johannesburg South Africa is acknowledged. The authors are also grateful to the Center for High Performance Computing (CHPC), Cape Town for computational resources provided.

Conflict of Interest

The authors declare no conflict of interest.

Keywords

environmental remediation, first-principles calculation, photocatalysis, semiconductors, water treatment

Received: January 23, 2017

Revised: February 26, 2017

Published online:

- [1] B. Pernet-Coudrier, W. Qi, H. Liu, B. Müller, M. Berg, *Environ. Sci. Technol.* **2012**, *46*, 5294.
- [2] M. Rafatullah, O. Sulaiman, R. Hashim, A. Ahmad, *J. Hazard. Mater.* **2010**, *177*, 70.
- [3] T.-W. Hao, P.-Y. Xiang, H. R. Mackey, K. Chi, H. Lu, H.-k. Chui, M. C. M. van Loosdrecht, G.-H. Chen, *Water Res.* **2014**, *65*, 1.
- [4] M. M. Pendergast, E. M. V. Hoek, *Energy Environ. Sci.* **2011**, *4*, 1946.
- [5] M. Catalá, N. Domínguez-Morueco, A. Migens, R. Molina, F. Martínez, Y. Valcárcel, N. Mastroianni, M. L. de Alda, D. Barceló, Y. Segura, *Sci. Total Environ.* **2015**, *520*, 198.
- [6] O. Ganzenko, D. Huguenot, E. D. Hullebusch, G. Esposito, M. A. Oturan, *Environ. Sci. Pollut. Res.* **2014**, *21*, 8493.
- [7] a) G. Wang, H. Yuan, A. Kuang, W. Hu, G. Zhang, H. Chen, *Int. J. Hydrogen Energy* **2014**, *39*, 3780; b) Y. Zhou, G. Chen, Y. Yu, Y. Feng, Y. Zheng, F. He, Z. Han, *Phys. Chem. Chem. Phys.* **2015**, *17*, 1870; c) H. Dong, G. Chen, J. Sun, C. Li, Y. Yu, D. Chen, *Appl. Catal., B* **2013**, *134*, 46; d) H. Dong, G. Chen, J. Sun, Y. Feng, C. Li, C. Lv, *Chem. Commun.* **2014**, *50*, 6596.
- [8] X. Qu, P. J. Alvarez, Q. Li, *Water Res.* **2013**, *47*, 3931.
- [9] a) C. Sousa, S. Tosoni, F. Illas, *Chem. Rev.* **2012**, *113*, 4456; b) A. V. Akimov, A. J. Neukirch, O. V. Prezhdo, *Chem. Rev.* **2013**, *113*, 4496.
- [10] B. M. Austin, D. Y. Zubarev, W. A. Lester Jr., *Chem. Rev.* **2011**, *112*, 263.
- [11] D. I. Lyakh, M. Musiał, V. F. Lotrich, R. J. Bartlett, *Chem. Rev.* **2011**, *112*, 182.
- [12] P. G. Szalay, T. Müller, G. Gidofalvi, H. Lischka, R. Shepard, *Chem. Rev.* **2011**, *112*, 108.
- [13] a) A. J. Cohen, P. Mori-Sánchez, W. Yang, *Chem. Rev.* **2011**, *112*, 289; b) J. K. Nørskov, F. Abild-Pedersen, F. Studt, T. Bligaard, *Proc. Natl. Acad. Sci. USA* **2011**, *108*, 937.
- [14] P. Hohenberg, W. Kohn, *Phys. Rev.* **1964**, *136*, B864.
- [15] W. Kohn, L. J. Sham, *Phys. Rev.* **1965**, *140*, A1133.
- [16] J. Perdew, A. Zunger, *Phys. Rev. B* **1981**, *23*, 5048.
- [17] J. P. Perdew, *Phys. Rev. B* **1986**, *33*, 8822.
- [18] J. P. Perdew, J. A. Chevary, S. H. Vosko, K. A. Jackson, M. R. Pederson, D. J. Singh, C. Fiolhais, *Phys. Rev. B* **1992**, *46*, 6671.
- [19] J. P. Perdew, K. Burke, M. Ernzerhof, *Phys. Rev. Lett.* **1996**, *77*, 3865.
- [20] B. Hammer, L. B. Hansen, J. K. Nørskov, *Phys. Rev. B* **1999**, *59*, 7413.
- [21] K. A. Johnson, N. Ashcroft, *Nature* **2000**, *403*, 632.
- [22] Z. Wu, R. Cohen, D. Singh, *Phys. Rev. B* **2004**, *70*, 104112.
- [23] J. Paier, M. Marsman, K. Hummer, G. Kresse, I. C. Gerber, J. G. Ángyán, *J. Chem. Phys.* **2006**, *124*, 154709.
- [24] J. Hafner, *J. Comput. Chem.* **2008**, *29*, 2044.
- [25] A. V. Krukau, O. A. Vydrov, A. F. Izmaylov, G. E. Scuseria, *J. Chem. Phys.* **2006**, *125*, 224106.
- [26] V. I. Anisimov, F. Aryasetiawan, A. Lichtenstein, *J. Phys.: Condens. Matter* **1997**, *9*, 767.
- [27] C. Franchini, R. Kováčik, M. Marsman, S. S. Murthy, J. He, C. Ederer, G. Kresse, *J. Phys.: Condens. Matter* **2012**, *24*, 235602.
- [28] X. Blase, C. Attaccalite, V. Olevano, *Phys. Rev. B* **2011**, *83*, 115103.
- [29] O. Kvyatkovskii, F. Karadag, A. Mamedov, G. Zakharov, *Phys. Solid State* **2004**, *46*, 1717.
- [30] H. Ishida, D. Wortmann, A. Liebsch, *Phys. Rev. B* **2006**, *73*, 245421.
- [31] a) G. Kresse, J. Furthmüller, *Phys. Rev. B* **1996**, *54*, 11169; b) G. Kresse, J. Furthmüller, *Comput. Mater. Sci.* **1996**, *6*, 15.
- [32] M. S. José, A. Emilio, D. G. Julian, G. Alberto, J. Javier, O. Pablo, S.-P. Daniel, *J. Phys.: Condens. Matter* **2002**, *14*, 2745.
- [33] S. Clark, M. Segall, C. Pickard, P. Hasnip, M. Probert, K. Refson, M. Payne, *Material Studio Cambridge Serial Total Energy Package (CASTEP), version 5.0*, Accelrys, San Diego, CA, **2009**.

- [34] a) B. Delley, *J. Chem. Phys.* **1990**, *92*, 508; b) B. Delley, *J. Phys. Chem. A* **1996**, *100*, 6107.
- [35] Y. Inoue, *Energy Environ. Sci.* **2009**, *2*, 364.
- [36] A. G. Tamirat, J. Rick, A. A. Dubale, W.-N. Su, B.-J. Hwang, *Nanoscale Horiz.* **2016**, *1*, 243.
- [37] M. Barroso, S. R. Pendlebury, A. J. Cowan, J. R. Durrant, *Chem. Sci.* **2013**, *4*, 2724.
- [38] M. N. Huda, A. Walsh, Y. Yan, S.-H. Wei, M. M. Al-Jassim, *J. Appl. Phys.* **2010**, *107*, 123712.
- [39] R. van de Krol, Y. Liang, J. Schoonman, *J. Mater. Chem.* **2008**, *18*, 2311.
- [40] B. A. Aragaw, C.-J. Pan, W.-N. Su, H.-M. Chen, J. Rick, B.-J. Hwang, *Appl. Catal., B* **2015**, *163*, 478.
- [41] M. D. Hernández-Alonso, F. Fresno, S. Suárez, J. M. Coronado, *Energy Environ. Sci.* **2009**, *2*, 1231.
- [42] D. O. Scanlon, C. W. Dunnill, J. Buckeridge, S. A. Shevlin, A. J. Logsdail, S. M. Woodley, C. R. A. Catlow, M. J. Powell, R. G. Palgrave, I. P. Parkin, G. W. Watson, T. W. Keal, P. Sherwood, A. Walsh, A. A. Sokol, *Nat. Mater.* **2013**, *12*, 798.
- [43] P. Luan, M. Xie, D. Liu, X. Fu, L. Jing, *Sci. Rep.* **2014**, *4*, 6189.
- [44] M. Bledowski, L. Wang, A. Ramakrishnan, O. V. Khavryuchenko, V. D. Khavryuchenko, P. C. Ricci, J. Strunk, T. Cremer, C. Kolbeck, R. Beranek, *Phys. Chem. Chem. Phys.* **2011**, *13*, 21511.
- [45] P.-Q. Wang, Y. Bai, P.-Y. Luo, J.-Y. Liu, *Catal. Commun.* **2013**, *38*, 82.
- [46] Y. Liu, Q. Li, S. Gao, J. K. Shang, *CrystEngComm* **2014**, *16*, 7493.
- [47] K. Ding, B. Chen, Y. Li, Y. Zhang, Z. Chen, *J. Mater. Chem. A* **2014**, *2*, 8294.
- [48] S. Huang, W. Luo, Z. Zou, *J. Phys. D: Appl. Phys.* **2013**, *46*, 235108.
- [49] C.-Y. Lee, Y.-T. Haung, W.-F. Su, C.-F. Lin, *Appl. Phys. Lett.* **2006**, *89*, 231116.
- [50] S. Chen, L.-W. Wang, *Chem. Mater.* **2012**, *24*, 3659.
- [51] P. D. Tran, V. Artero, M. Fontecave, *Energy Environ. Sci.* **2010**, *3*, 727.
- [52] T. Hisatomi, J. Kubota, K. Domen, *Chem. Soc. Rev.* **2014**, *43*, 7520.
- [53] J. Pan, Z. Wang, Q. Chen, J. Hu, J. Wang, *Nanoscale* **2014**, *6*, 13565.
- [54] K. Nakaoka, J. Ueyama, K. Ogura, *J. Electrochem. Soc.* **2004**, *151*, C661.
- [55] M. Grätzel, *Nature* **2001**, *414*, 338.
- [56] A. Paracchino, V. Laporte, K. Sivula, M. Grätzel, E. Thimsen, *Nat. Mater.* **2011**, *10*, 456.
- [57] X.-W. Liu, W.-W. Li, H.-Q. Yu, *Chem. Soc. Rev.* **2014**, *43*, 7718.
- [58] A. Kudo, Y. Miseki, *Chem. Soc. Rev.* **2009**, *38*, 253.
- [59] S. Kim, J. Choi, M. Jung, S. Joo, S. Kim, *Sensors* **2013**, *13*, 13575.
- [60] S. Kohtani, E. Yoshioka, H. Miyabe, in *Hydrogenation* (Ed: I. Karamé), InTech, Kobe, Japan **2012**, p. 291.
- [61] A. Ganguly, O. Anjaneyulu, K. Ojha, A. K. Ganguli, *CrystEngComm* **2015**, *17*, 8978.
- [62] A. J. Bard, L. R. Faulkner, *Fundamentals and Applications*, 2nd ed., Wiley, New York **2001**.
- [63] U. I. Gaya, A. H. Abdullah, *J. Photochem. Photobiol., C* **2008**, *9*, 1.
- [64] M. N. Chong, B. Jin, C. W. K. Chow, C. Saint, *Water Res.* **2010**, *44*, 2997.
- [65] Y. Chen, K. Zhang, Y. Zuo, *Sci. Total Environ.* **2013**, *463*, 802.
- [66] P. Niu, Y. Yang, C. Y. Jimmy, G. Liu, H.-M. Cheng, *Chem. Commun.* **2014**, *50*, 10837.
- [67] a) J. Warren, C. Perkins, K. Jelfs, P. Boldrin, P. Chater, G. Miller, T. Manning, M. Briggs, K. Stylianou, J. Claridge, *Angew. Chem.* **2014**, *126*, 4680; b) X. Zhao, X. Bu, T. Wu, S.-T. Zheng, L. Wang, P. Feng, *Nat. Commun.* **2013**, *4*, 2344.
- [68] a) M.-V. Sofianou, V. Psycharis, N. Boukos, T. Vaimakis, J. Yu, R. Dillert, D. Bahnemann, C. Trapalis, *Appl. Catal., B* **2013**, *142*, 761; b) W. J. Tseng, R.-D. Lin, *J. Colloid Interface Sci.* **2014**, *428*, 95.
- [69] a) R. Negishi, S.-i. Naya, H. Tada, *J. Phys. Chem. C* **2015**, *119*, 11771; b) X. Wang, N. Chen, G. Liu, A. T. X. Sha, K. Ma, *Inorg. Chim. Acta* **2015**, *432*, 128; c) F. Yanfen, H. Yingping, Y. Jing, W. Pan, C. Genwei, *Environ. Sci. Technol.* **2011**, *45*, 1593.
- [70] A. Fujishima, K. Honda, *Nature* **1972**, *238*, 37.
- [71] A. Y. Ahmed, T. A. Kandiel, T. Oekermann, D. Bahnemann, *J. Phys. Chem. Lett.* **2011**, *2*, 2461.
- [72] R. Wei, J. Hu, T. Zhou, X. Zhou, J. Liu, J. Li, *Acta Mater.* **2014**, *66*, 163.
- [73] a) X. Zhang, J. Qin, Y. Xue, P. Yu, B. Zhang, L. Wang, R. Liu, *Sci. Rep.* **2014**, *4*, 4596; b) S. O. B. Oppong, W. W. Anku, S. K. Shukla, P. P. Govender, *Res. Chem. Intermed.* **2017**, *43*, 481.
- [74] W. Wang, J. Wang, Z. Wang, X. Wei, L. Liu, Q. Ren, W. Gao, Y. Liang, H. Shi, *Dalton Trans.* **2014**, *43*, 6735.
- [75] S. Zhuang, X. Xu, Y. Pang, J. Hu, C. Yang, L. Tong, Y. Zhou, *RSC Adv.* **2013**, *3*, 20422.
- [76] S. Zhang, *Ceram. Int.* **2014**, *40*, 4553.
- [77] H. Cheng, B. Huang, Y. Dai, *Nanoscale* **2014**, *6*, 2009.
- [78] K. Wang, J. Xu, X. Hua, N. Li, M. Chen, F. Teng, Y. Zhu, W. Yao, *J. Mol. Catal. A: Chem.* **2014**, *393*, 302.
- [79] Z. Dai, F. Qin, H. Zhao, J. Ding, Y. Liu, R. Chen, *ACS Catal.* **2016**, *6*, 3180.
- [80] J. Cao, B. Luo, H. Lin, B. Xu, S. Chen, *Appl. Catal., B* **2012**, *111–112*, 288.
- [81] H. Lin, H. Ye, B. Xu, J. Cao, S. Chen, *Catal. Commun.* **2013**, *37*, 55.
- [82] a) J. Wang, S. Su, B. Liu, M. Cao, C. Hu, *Chem. Commun.* **2013**, *49*, 7830; b) H. Kato, A. Kudo, *J. Phys. Chem. B* **2001**, *105*, 4285.
- [83] S. Dong, J. Sun, Y. Li, C. Yu, Y. Li, J. Sun, *Appl. Catal., B* **2014**, *144*, 386.
- [84] H. Liu, J. Yuan, W. Shangguan, Y. Teraoka, *J. Phys. Chem. C* **2008**, *112*, 8521.
- [85] B. Ma, J. Yang, H. Han, J. Wang, X. Zhang, C. Li, *J. Phys. Chem. C* **2010**, *114*, 12818.
- [86] K. Saito, K. Koga, A. Kudo, *Dalton Trans.* **2011**, *40*, 3909.
- [87] G.-F. Huang, Z.-L. Ma, W.-Q. Huang, Y. Tian, C. Jiao, Z.-M. Yang, Z. Wan, A. Pan, *J. Nanomater.* **2013**, *2013*, 1.
- [88] F. E. Osterloh, *Chem. Mater.* **2008**, *20*, 35.
- [89] H. Dong, Z. Li, X. Xu, Z. Ding, L. Wu, X. Wang, X. Fu, *Appl. Catal., B* **2009**, *89*, 551.
- [90] a) E. S. Agorku, A. C. Pandey, B. B. Mamba, A. K. Mishra, *Mater. Today* **2015**, *2*, 3909; b) W. W. Anku, S. O.-B. Oppong, S. K. Shukla, E. S. Agorku, P. P. Govender, *Appl. Phys. A* **2016**, *122*, 579.
- [91] M. Tabata, K. Maeda, T. Ishihara, T. Minegishi, T. Takata, K. Domen, *J. Phys. Chem. C* **2010**, *114*, 11215.
- [92] J. Hong, Y. Wang, Y. Wang, W. Zhang, R. Xu, *ChemSusChem* **2013**, *6*, 2263.
- [93] Y.-P. Yuan, S.-W. Cao, L.-S. Yin, L. Xu, C. Xue, *Int. J. Hydrogen Energy* **2013**, *38*, 7218.
- [94] L. Zhang, T. Jiang, S. Li, Y. Lu, L. Wang, X. Zhang, D. Wang, T. Xie, *Dalton Trans.* **2013**, *42*, 12998.
- [95] M. Nguyen, P. D. Tran, S. S. Pramana, R. L. Lee, S. K. Batabyal, N. Mathews, L. H. Wong, M. Graetzel, *Nanoscale* **2013**, *5*, 1479.
- [96] M. L. Tang, D. C. Grauer, B. Lassalle-Kaiser, V. K. Yachandra, L. Amirav, J. R. Long, J. Yano, A. P. Alivisatos, *Angew. Chem., Int. Ed.* **2011**, *50*, 10203.
- [97] X. Zong, J. Han, G. Ma, H. Yan, G. Wu, C. Li, *J. Phys. Chem. C* **2011**, *115*, 12202.
- [98] S. Nazir, M. Upadhyay Kahaly, U. Schwingenschlögl, *Appl. Phys. Lett.* **2012**, *100*, 201607.
- [99] T. Hayashi, M. Deura, K. Ohkawa, *Jpn. J. Appl. Phys.* **2012**, *51*, 112601.
- [100] H. Katsumata, T. Sakai, T. Suzuki, S. Kaneco, *Ind. Eng. Chem. Res.* **2014**, *53*, 8018.
- [101] K. Maeda, N. Saito, D. Lu, Y. Inoue, K. Domen, *J. Phys. Chem. C* **2007**, *111*, 4749.
- [102] R. Li, Z. Chen, W. Zhao, F. Zhang, K. Maeda, B. Huang, S. Shen, K. Domen, C. Li, *J. Phys. Chem. C* **2012**, *117*, 376.

- [103] M. Tabata, K. Maeda, M. Higashi, D. Lu, T. Takata, R. Abe, K. Domen, *Langmuir* **2010**, *26*, 9161.
- [104] Y. Chen, S. Liang, L. Wen, W. Wu, R. Yuan, X. Wang, L. Wu, *Phys. Chem. Chem. Phys.* **2013**, *15*, 12742.
- [105] W. Lü, Y. Wu, J. Chen, Y. Yang, *CrystEngComm* **2014**, *16*, 609.
- [106] a) L. Liu, J. Hensel, R. C. Fitzmorris, Y. Li, J. Z. Zhang, *J. Phys. Chem. Lett.* **2010**, *1*, 155; b) C. Wang, R. L. Thompson, J. Baltrus, C. Matrangola, *J. Phys. Chem. Lett.* **2010**, *1*, 48; c) L. Huang, X. Wang, J. Yang, G. Liu, J. Han, C. Li, *J. Phys. Chem. C* **2013**, *117*, 11584.
- [107] M. Ye, M. Wang, D. Zheng, N. Zhang, C. Lin, Z. Lin, *Nanoscale* **2014**, *6*, 3576.
- [108] A. K. Agegnehu, C.-J. Pan, J. Rick, J.-F. Lee, W.-N. Su, B.-J. Hwang, *J. Mater. Chem.* **2012**, *22*, 13849.
- [109] D. Praveen Kumar, M. V. Shankar, M. Mamatha Kumari, G. Sadanandam, B. Srinivas, V. Durgakumari, *Chem. Commun.* **2013**, *49*, 9443.
- [110] D. Chen, J. Ye, *Chem. Mater.* **2009**, *21*, 2327.
- [111] A. Kudo, H. Kato, S. Nakagawa, *J. Phys. Chem. B* **2000**, *104*, 571.
- [112] L. Zeng, W. Ren, L. Xiang, J. Zheng, B. Chen, A. Wu, *Nanoscale* **2013**, *5*, 2107.
- [113] K.-i. Katsumata, C. E. J. Cordonier, T. Shichi, A. Fujishima, *J. Am. Chem. Soc.* **2009**, *131*, 3856.
- [114] D. Wang, Y. Duan, Q. Luo, X. Li, L. Bao, *Desalination* **2011**, *270*, 174.
- [115] S. H. Kim, S. Park, C. W. Lee, B. S. Han, S. W. Seo, J. S. Kim, I. S. Cho, K. S. Hong, *Int. J. Hydrogen Energy* **2012**, *37*, 16895.
- [116] Z. Wan, G. Zhang, J. Wang, Y. Zhang, *RSC Adv.* **2013**, *3*, 19617.
- [117] Z. Zhang, P. Wang, *Energy Environ. Sci.* **2012**, *5*, 6506.
- [118] K. van Benthem, C. Elsässer, R. H. French, *J. Appl. Phys.* **2001**, *90*, 6156.
- [119] Ü. Özgür, Y. I. Alivov, C. Liu, A. Teke, M. A. Reshchikov, S. Doğan, V. Avrutin, S.-J. Cho, H. Morkoç, *J. Appl. Phys.* **2005**, *98*, 041301.
- [120] K.-L. Zhang, C.-M. Liu, F.-Q. Huang, C. Zheng, W.-D. Wang, *Appl. Catal., B* **2006**, *68*, 125.
- [121] A. Emeline, G. V. Kataeva, A. S. Litke, A. V. Rudakova, V. K. Ryabchuk, N. Serpone, *Langmuir* **1998**, *14*, 5011.
- [122] a) E. Vella, F. Messina, M. Cannas, R. Boscaino, *Phys. Rev. B* **2011**, *83*, 174201; b) G. Hautier, A. Miglio, G. Ceder, G.-M. Rignanese, X. Gonze, *Nat. Commun.* **2013**, *4*, 2292.
- [123] X. Chen, S. Shen, L. Guo, S. S. Mao, *Chem. Rev.* **2010**, *110*, 6503.
- [124] Q. Wu, R. van de Krol, *J. Am. Chem. Soc.* **2012**, *134*, 9369.
- [125] J. Lu, F. Su, Z. Huang, C. Zhang, Y. Liu, X. Ma, J. Gong, *RSC Adv.* **2013**, *3*, 720.
- [126] H. Tada, M. Fujishima, H. Kobayashi, *Chem. Soc. Rev.* **2011**, *40*, 4232.
- [127] A. C. B. Silva, V. C. Costa, J. D. Ardisson, F. Magalhães, R. M. Lago, M. T. C. Sansiviero, *Mater. Res. Bull.* **2010**, *45*, 174.
- [128] a) S. Zhang, S.-H. Wei, A. Zunger, *Phys. B: Condens. Matter* **1999**, *273*, 976; b) W. Walukiewicz, *Phys. B: Condens. Matter* **2001**, *302*, 123.
- [129] R. Asahi, T. Morikawa, T. Ohwaki, K. Aoki, Y. Taga, *Science* **2001**, *293*, 269.
- [130] S. Dong, J. Feng, M. Fan, Y. Pi, L. Hu, X. Han, M. Liu, J. Sun, J. Sun, *RSC Adv.* **2015**, *5*, 14610.
- [131] a) J. Zhang, Q. Xu, S. Z. Qiao, J. Yu, *ChemSusChem* **2013**, *6*, 2009; b) E. S. Agorku, M. A. Mamo, B. B. Mamba, A. C. Pandey, A. K. Mishra, *J. Porous Mater.* **2014**, *22*, 47.
- [132] P. Kanhere, Y. Tang, J. Zheng, Z. Chen, *J. Phys. Chem. Solids* **2013**, *74*, 1708.
- [133] L. M. Torres-Martínez, R. Gómez, O. Vázquez-Cuchillo, I. Juárez-Ramírez, A. Cruz-López, F. J. Alejandro-Sandoval, *Catal. Commun.* **2010**, *12*, 268.
- [134] a) L. Liu, P. Li, B. Adisak, S. Ouyang, N. Umezawa, J. Ye, R. Kodiyath, T. Tanabe, G. V. Ramesh, S. Ueda, H. Abe, *J. Mater. Chem. A* **2014**, *2*, 9875; b) S. Kawasaki, R. Takahashi, K. Akagi, J. Yoshinobu, F. Komori, K. Horiba, H. Kumigashira, K. Iwashina, A. Kudo, M. Lippmaa, *J. Phys. Chem. C* **2014**, *118*, 20222.
- [135] a) B. K. Avsarala, S. R. Tirukkavalluri, S. Bojja, *Int. J. Mater. Res.* **2010**, *101*, 1563; b) U. G. Akpan, B. H. Hameed, *J. Colloid Interface Sci.* **2011**, *357*, 168.
- [136] a) L. She, G. Tan, H. Ren, J. Huang, C. Xu, A. Xia, *RSC Adv.* **2015**, *5*, 36642; b) J. Tao, M. Yang, J. W. Chai, J. S. Pan, Y. P. Feng, S. J. Wang, *J. Phys. Chem. C* **2014**, *118*, 994.
- [137] a) Y. Xie, C. Yuan, *Appl. Catal., B* **2003**, *46*, 251; b) E. S. Agorku, H. Mittal, B. B. Mamba, A. C. Pandey, A. K. Mishra, *Int. J. Biol. Macromol.* **2014**, *70*, 143.
- [138] N. Murakami, T. Chiyoya, T. Tsubota, T. Ohno, *Appl. Catal., A* **2008**, *348*, 148.
- [139] J. O. Sofo, A. S. Chaudhari, G. D. Barber, *Phys. Rev. B* **2007**, *75*, 153401.
- [140] J. Li, T. Zhao, T. Chen, Y. Liu, C. N. Ong, J. Xie, *Nanoscale* **2015**, *7*, 7502.
- [141] I. Tsuji, H. Kato, A. Kudo, *Angew. Chem.* **2005**, *117*, 3631.
- [142] Q. Wang, T. Hisatomi, S. S. K. Ma, Y. Li, K. Domen, *Chem. Mater.* **2014**, *26*, 4144.
- [143] a) F. N. Sayed, O. Jayakumar, R. Sasikala, R. Kadam, S. R. Bharadwaj, L. Kienle, U. Schürmann, S. r. Kaps, R. Adelung, J. Mittal, *J. Phys. Chem. C* **2012**, *116*, 12462; b) W. W. Anku, S. O.-B. Oppong, S. K. Shukla, E. S. Agorku, P. P. Govender, *Appl. Phys. A* **2016**, *122*, 1.
- [144] a) S. Lingampalli, U. K. Gautam, C. Rao, *Energy Environ. Sci.* **2013**, *6*, 3589; b) K. Wu, H. Zhu, Z. Liu, W. Rodríguez-Córdoba, T. Lian, *J. Am. Chem. Soc.* **2012**, *134*, 10337.
- [145] F. Wang, Y. Jiang, A. Gautam, Y. Li, R. Amal, *ACS Catal.* **2014**, *4*, 1451.
- [146] C. Zhao, A. Krall, H. Zhao, Q. Zhang, Y. Li, *Int. J. Hydrogen Energy* **2012**, *37*, 9967.
- [147] J. Yang, D. Wang, H. Han, C. Li, *Acc. Chem. Res.* **2013**, *46*, 1900.
- [148] P. D. Tran, L. Xi, S. K. Batabyal, L. H. Wong, J. Barber, J. S. C. Loo, *Phys. Chem. Chem. Phys.* **2012**, *14*, 11596.
- [149] W. Wang, S. Liu, L. Nie, B. Cheng, J. Yu, *Phys. Chem. Chem. Phys.* **2013**, *15*, 12033.
- [150] W. J. Foo, C. Zhang, G. W. Ho, *Nanoscale* **2013**, *5*, 759.
- [151] A.-W. Xu, Y. Gao, H.-Q. Liu, *J. Catal.* **2002**, *207*, 151.
- [152] D. J. Singh, L. Nordstrom, *Planewaves, Pseudopotentials, and the LAPW Method*, Springer Science & Business Media, New York, NY, **2006**.
- [153] P. E. Blöchl, *Phys. Rev. B* **1994**, *50*, 17953.
- [154] W. E. Pickett, *Comput. Phys. Rep.* **1989**, *9*, 115.
- [155] O. F. Sankey, R. W. Jansen, *J. Vac. Sci. Technol.* **1988**, *6*, 1240.
- [156] W. M. Mulwa, C. N. M. Ouma, M. O. Onani, F. B. Dejene, *J. Solid State Chem.* **2016**, *237*, 129.
- [157] Y. Yalçın, M. Kılıç, Z. Çınar, *Appl. Catal., B* **2010**, *99*, 469.
- [158] L. Wen, B. Liu, X. Zhao, K. Nakata, T. Murakami, A. Fujishima, *Int. J. Photoenergy* **2012**, *2012*, 10.
- [159] J.-J. Chen, W.-K. Wang, W.-W. Li, D.-N. Pei, H.-Q. Yu, *ACS Appl. Mater. Interfaces* **2015**, *7*, 12671.
- [160] M. Guo, J. Du, *Phys. B: Condens. Matter* **2012**, *407*, 1003.
- [161] J. Navas, A. Sánchez-Coronilla, T. Aguilar, N. C. Hernández, M. Desirée, J. Sánchez-Márquez, D. Zorrilla, C. Fernández-Lorenzo, R. Alcántara, J. Martín-Calleja, *Phys. Chem. Chem. Phys.* **2014**, *16*, 3835.
- [162] Y.-M. Lin, Z.-Y. Jiang, C.-Y. Zhu, X.-Y. Hu, X.-D. Zhang, *J. Fan, Mater. Chem. Phys.* **2012**, *133*, 746.
- [163] M. Khan, J. Xu, W. Cao, Z.-K. Liu, *J. Nanosci. Nanotechnol.* **2014**, *14*, 6865.
- [164] P. Reunchan, N. Umezawa, S. Ouyang, J. Ye, *Phys. Chem. Chem. Phys.* **2012**, *14*, 1876.
- [165] K. E. Kweon, G. S. Hwang, J. Kim, S. Kim, S. Kim, *Phys. Chem. Chem. Phys.* **2015**, *17*, 256.

- [166] J. K. Cooper, S. Gul, F. M. Toma, L. Chen, P.-A. Glans, J. Guo, J. W. Ager, J. Yano, I. D. Sharp, *Chem. Mater.* **2014**, *26*, 5365.
- [167] K. Ding, L. Wen, L. Xu, H. Wu, Y. Ye, Y. Zhang, *Int. J. Quantum Chem.* **2016**, *116*, 388.
- [168] K. Ding, B. Chen, Z. Fang, Y. Zhang, Z. Chen, *Phys. Chem. Chem. Phys.* **2014**, *16*, 13465.
- [169] Z. Zhao, W. Luo, Z. Li, Z. Zou, *Phys. Lett. A* **2010**, *374*, 4919.
- [170] F. Wang, K. Cao, Y. Wu, K.-H. Zhang, Y. Zhou, *Appl. Surf. Sci.* **2016**, *360* (Part B), 1075.
- [171] X. Ma, Y. Dai, M. Guo, B. Huang, *ChemPhysChem* **2012**, *13*, 2304.
- [172] a) J. Zhu, Z. Deng, F. Chen, J. Zhang, H. Chen, M. Anpo, J. Huang, L. Zhang, *Appl. Catal., B* **2006**, *62*, 329; b) H. Yamashita, M. Harada, J. Misaka, M. Takeuchi, K. Ikeue, M. Anpo, *J. Photochem. Photobiol., A: Chem.* **2002**, *148*, 257.
- [173] W. Choi, A. Termin, M. R. Hoffmann, *J. Phys. Chem. A* **1994**, *98*, 13669.
- [174] M. L. Guo, X. D. Zhang, C. T. Liang, *Phys. B: Condens. Matter* **2011**, *406*, 3354.
- [175] J. Wang, D. N. Tafen, J. P. Lewis, Z. Hong, A. Manivannan, M. Zhi, M. Li, N. Wu, *J. Am. Chem. Soc.* **2009**, *131*, 12290.
- [176] a) C. Sun, A. Mukherji, G. Liu, L. Wang, S. C. Smith, *Chem. Phys. Lett.* **2011**, *501*, 427; b) J. B. Varley, A. Janotti, C. G. Van de Walle, *Adv. Mater.* **2011**, *23*, 2343.
- [177] a) F. Wang, D. Li, *Mater. Lett.* **2015**, *158*, 119; b) S. W. Shin, J. Y. Lee, K.-S. Ahn, S. H. Kang, J. H. Kim, *J. Phys. Chem. C* **2015**, *119*, 13375.
- [178] Y. Komai, K. Okitsu, R. Nishimura, N. Ohtsu, G. Miyamoto, T. Furuhashi, S. Semboshi, Y. Mizukoshi, N. Masahashi, *Catal. Today* **2011**, *164*, 399.
- [179] a) Z. Hua, Z. Dai, X. Bai, Z. Ye, H. Gu, X. Huang, *J. Hazard. Mater.* **2015**, *293*, 112; b) R. Ramanathan, V. Bansal, *RSC Adv.* **2015**, *5*, 1424.
- [180] a) H. F. Liu, *Solid State Commun.* **2012**, *152*, 2063; b) P. Liu, J. Nisar, B. Pathak, R. Ahuja, *Int. J. Hydrogen Energy* **2012**, *37*, 11611.
- [181] J. Sun, X. Zhao, H. Sun, W. Fan, *J. Solid State Chem.* **2012**, *194*, 352.
- [182] Y. Y. Gurkan, E. Kasapbasi, Z. Cinar, *Chem. Eng. J.* **2013**, *214*, 34.
- [183] Tian, Liu, *J. Phys. Chem. B* **2006**, *110*, 17866.
- [184] R. Liu, X. Zhou, F. Yang, Y. Yu, *Appl. Surf. Sci.* **2014**, *319*, 50.
- [185] W. Guo, Y. Guo, H. Dong, X. Zhou, *Phys. Chem. Chem. Phys.* **2015**, *17*, 5817.
- [186] K. Srinivasu, B. Modak, S. K. Ghosh, *J. Phys. Chem. C* **2014**, *118*, 26479.
- [187] W. Hao, P. L. James, *J. Phys.: Condens. Matter* **2005**, *17*, L209.
- [188] Y. Guo, X. Qiu, H. Dong, X. Zhou, *Phys. Chem. Chem. Phys.* **2015**, *17*, 21611.
- [189] Y. Mi, S. Wang, J. Chai, J. Pan, C. Huan, Y. Feng, C. Ong, *Appl. Phys. Lett.* **2006**, *89*, 231992.
- [190] C. Zhang, Y. Jia, Y. Jing, Y. Yao, J. Ma, J. Sun, *Comput. Mater. Sci.* **2013**, *79*, 69.
- [191] H.-C. Chen, C.-W. Huang, J. C. S. Wu, S.-T. Lin, *J. Phys. Chem. C* **2012**, *116*, 7897.
- [192] K. Yang, Y. Dai, B. Huang, *J. Phys. Chem. C* **2007**, *111*, 18985.
- [193] a) M. N. Uddin, M. S. Islam, M. M. R. Mazumder, M. A. Hossain, M. Elias, I. A. Siddiquey, M. A. B. H. Susan, D. K. Saha, M. M. Rahman, A. M. Asiri, S. Hayami, *J. Incl. Phenom. Macrocycl. Chem.* **2015**, *82*, 229; b) W. Anku, S. O.-B. Oppong, S. K. Shukla, P. P. Govender, *Acta Chim. Slov.* **2016**, *63*, 380.
- [194] Y. Jiang, H. Yuan, H. Chen, *Phys. Chem. Chem. Phys.* **2015**, *17*, 630.
- [195] Y. Wu, M. Xing, J. Zhang, F. Chen, *Appl. Catal., B* **2010**, *97*, 182.
- [196] F. Amano, K. Nogami, B. Ohtani, *Catal. Commun.* **2012**, *20*, 12.
- [197] S. In, A. Orlov, R. Berg, F. García, S. Pedrosa-Jimenez, M. S. Tikhov, D. S. Wright, R. M. Lambert, *J. Am. Chem. Soc.* **2007**, *129*, 13790.
- [198] H. Li, L. Chen, S. Liu, C. Li, J. Meng, Z. Wang, *Mater. Sci.- Pol.* **2015**, *33*, 549.
- [199] Y. Gai, J. Li, S.-S. Li, J.-B. Xia, S.-H. Wei, *Phys. Rev. Lett.* **2009**, *102*, 036402.
- [200] M. N. Uddin, S. U. A. Shibly, R. Ovali, I. Saiful, M. M. R. Mazumder, M. S. Islam, M. J. Uddin, O. Gulseren, E. Bengu, *J. Photochem. Photobiol., A: Chem.* **2013**, *254*, 25.
- [201] M. E. Kurtoglu, T. Longenbach, K. Sohlberg, Y. Gogotsi, *J. Phys. Chem. C* **2011**, *115*, 17392.
- [202] Q. Meng, T. Wang, E. Liu, X. Ma, Q. Ge, J. Gong, *Phys. Chem. Chem. Phys.* **2013**, *15*, 9549.
- [203] Y.-M. Lin, Z.-Y. Jiang, X.-Y. Hu, X.-D. Zhang, J. Fan, H. Miao, Y.-B. Shang, *Chin. Phys. B* **2012**, *21*, 033103.
- [204] Z. Jiang, Y. Lin, T. Mei, X. Hu, W. Chen, R. Ji, E. Liu, R. Zhang, L. Zhang, Q. Zhang, B. Zhou, D. Zhang, J. Fan, H. Zhu, X. Zhang, S. Wan, S. Zhu, Y. Shang, *Comput. Mater. Sci.* **2013**, *68*, 234.
- [205] J. Yu, P. Zhou, Q. Li, *Phys. Chem. Chem. Phys.* **2013**, *15*, 12040.
- [206] M. Guo, *RSC Adv.* **2015**, *5*, 434.
- [207] K. Yang, W.-Q. Huang, L. Xu, K.-W. Luo, Y.-C. Yang, G.-F. Huang, *Mater. Sci. Semicond. Process.* **2016**, *41*, 200.
- [208] W. Wei, Y. Dai, M. Guo, L. Yu, H. Jin, S. Han, B. Huang, *Phys. Chem. Chem. Phys.* **2010**, *12*, 7612.
- [209] B. Modak, S. K. Ghosh, *J. Phys. Chem. B* **2015**, *119*, 11089.
- [210] B. Modak, K. Srinivasu, S. K. Ghosh, *Phys. Chem. Chem. Phys.* **2014**, *16*, 24527.
- [211] B. Modak, K. Srinivasu, S. K. Ghosh, *J. Phys. Chem. C* **2014**, *118*, 10711.
- [212] B. Modak, S. K. Ghosh, *J. Phys. Chem. C* **2015**, *119*, 23503.
- [213] B. Modak, K. Srinivasu, S. K. Ghosh, *RSC Adv.* **2014**, *4*, 45703.
- [214] P. Kanhere, J. Nisar, Y. Tang, B. Pathak, R. Ahuja, J. Zheng, Z. Chen, *J. Phys. Chem. C* **2012**, *116*, 22767.
- [215] G.-Z. Wang, H. Chen, G. Wu, A.-L. Kuang, H.-K. Yuan, *ChemPhysChem* **2016**, *17*, 489.
- [216] G. Wang, H. Chen, Y. Li, A. Kuang, H. Yuan, G. Wu, *Phys. Chem. Chem. Phys.* **2015**, *17*, 28743.
- [217] M. Chhowalla, H. S. Shin, G. Eda, L.-J. Li, K. P. Loh, H. Zhang, *Nat. Chem.* **2013**, *5*, 263.
- [218] B. Modak, S. K. Ghosh, *RSC Adv.* **2016**, *6*, 9958.
- [219] Y. Lin, Z. Jiang, R. Zhang, C. Zhu, X. Hu, X. Zhang, H. Zhu, *J. Catal.* **2014**, *309*, 115.
- [220] K. Ding, L. Wen, M. Huang, Y. Zhang, Y. Lu, Z. Chen, *Phys. Chem. Chem. Phys.* **2016**, *18*, 19217.
- [221] J. Zhang, M. Deng, F. Ren, Y. Wu, Y. Wang, *RSC Adv.* **2016**, *6*, 12290.
- [222] H. S. Park, K. E. Kweon, H. Ye, E. Paek, G. S. Hwang, A. J. Bard, *J. Phys. Chem. C* **2011**, *115*, 17870.
- [223] Y. Li, K. Ding, B. Cheng, Y. Zhang, Y. Lu, *Phys. Chem. Chem. Phys.* **2015**, *17*, 5613.
- [224] M. Li, J. Zhang, W. Dang, S. K. Cushing, D. Guo, N. Wu, P. Yin, *Phys. Chem. Chem. Phys.* **2013**, *15*, 16220.
- [225] J. Qiu, S. Zhang, H. Zhao, *J. Hazard. Mater.* **2012**, *211–212*, 381.
- [226] M. Fujishima, Q. Jin, H. Yamamoto, H. Tada, M. Nolan, *Phys. Chem. Chem. Phys.* **2012**, *14*, 705.
- [227] H. Tada, Q. Jin, H. Nishijima, H. Yamamoto, M. Fujishima, S.-i. Okuoka, T. Hattori, Y. Sumida, H. Kobayashi, *Angew. Chem., Int. Ed.* **2011**, *50*, 3501.
- [228] J. A. Libera, J. W. Elam, N. F. Sather, T. Rajh, N. M. Dimitrijevic, *Chem. Mater.* **2010**, *22*, 409.
- [229] J. Tian, Z. Zhao, A. Kumar, R. I. Boughton, H. Liu, *Chem. Soc. Rev.* **2014**, *43*, 6920.
- [230] C. Yang, Y. Huang, F. Li, T. Li, *J. Mater. Sci.* **2016**, *51*, 1032.
- [231] P. Gomathisankar, K. Hachisuka, H. Katsumata, T. Suzuki, K. Funasaka, S. Kaneco, *Int. J. Hydrogen Energy* **2013**, *38*, 8625.
- [232] C. Liu, P. Li, G. Wu, B. Luo, S. Lin, A. Ren, W. Shi, *RSC Adv.* **2015**, *5*, 33938.

- [233] S. Hernandez, D. Hidalgo, A. Sacco, A. Chiodoni, A. Lamberti, V. Cauda, E. Tresso, G. Saracco, *Phys. Chem. Chem. Phys.* **2015**, *17*, 7775.
- [234] J. Liu, L. Zhang, N. Li, Q. Tian, J. Zhou, Y. Sun, *J. Mater. Chem. A* **2015**, *3*, 706.
- [235] C. Li, S. Wang, T. Wang, Y. Wei, P. Zhang, J. Gong, *Small* **2014**, *10*, 2783.
- [236] S. G. Ghugal, S. S. Umare, R. Sasikala, *RSC Adv.* **2015**, *5*, 63393.
- [237] Y.-S. Xu, W.-D. Zhang, *Appl. Catal., B* **2013**, *140–141*, 306.
- [238] L. Kong, Z. Jiang, T. Xiao, L. Lu, M. O. Jones, P. P. Edwards, *Chem. Commun.* **2011**, *47*, 5512.
- [239] I. Grigioni, K. G. Stamplecoskie, E. Selli, P. V. Kamat, *J. Phys. Chem. C* **2015**, *119*, 20792.
- [240] T. Cao, Y. Li, C. Wang, Z. Zhang, M. Zhang, C. Shao, Y. Liu, *J. Mater. Chem.* **2011**, *21*, 6922.
- [241] V. B. R. Boppana, R. F. Lobo, *ACS Catal.* **2011**, *1*, 923.
- [242] W. Yang, Y. Wen, D. Zeng, Q. Wang, R. Chen, W. Wang, B. Shan, *J. Mater. Chem. A* **2014**, *2*, 20770.
- [243] a) J. Bandara, S. Kuruppu, U. Pradeep, *Colloids Surf., A* **2006**, *276*, 197; b) H. Tada, M. Yamamoto, S. Ito, *J. Electrochem. Soc.* **2000**, *147*, 613.
- [244] M. Nolan, *ACS Appl. Mater. Interfaces* **2012**, *4*, 5863.
- [245] a) P. R. Keating, D. O. Scanlon, B. J. Morgan, N. M. Galea, G. W. Watson, *J. Phys. Chem. C* **2012**, *116*, 2443; b) B. J. Morgan, G. W. Watson, *J. Phys. Chem. C* **2010**, *114*, 2321.
- [246] A. Lucid, A. Iwaszuk, M. Nolan, *Mater. Sci. Semicond. Process.* **2014**, *25*, 59.
- [247] M. Nolan, *Phys. Chem. Chem. Phys.* **2011**, *13*, 18194.
- [248] A. Iwaszuk, M. Nolan, *J. Mater. Chem. A* **2013**, *1*, 6670.
- [249] A. Iwaszuk, A. K. Lucid, K. M. Razeeb, M. Nolan, *J. Mater. Chem. A* **2014**, *2*, 18796.
- [250] A. Iwaszuk, M. Nolan, *Catal. Sci. Technol.* **2013**, *3*, 2000.
- [251] A. Iwaszuk, P. A. Mulheran, M. Nolan, *J. Mater. Chem. A* **2013**, *1*, 2515.
- [252] J. Liu, *J. Phys. Chem. C* **2015**, *119*, 28417.
- [253] R. Chen, J. Zhu, H. An, F. Fan, C. Li, *Faraday Discuss.* **2016**.
- [254] Z. Zhang, J. T. Yates Jr., *Chem. Rev.* **2012**, *112*, 5520.
- [255] Y. Yang, J. Gu, J. L. Young, E. M. Miller, J. A. Turner, N. R. Neale, M. C. Beard, *Science* **2015**, *350*, 1061.
- [256] S. J. Moniz, S. A. Shevlin, D. J. Martin, Z.-X. Guo, J. Tang, *Energy Environ. Sci.* **2015**, *8*, 731.
- [257] J. Zhang, F. Ren, M. Deng, Y. Wang, *Phys. Chem. Chem. Phys.* **2015**, *17*, 10218.
- [258] S. Grimme, S. Ehrlich, L. Goerigk, *J. Comput. Chem.* **2011**, *32*, 1456.
- [259] A. D. Becke, E. R. Johnson, *J. Chem. Phys.* **2005**, *123*, 154101.
- [260] J. Wang, Z. Guan, J. Huang, Q. Li, J. Yang, *J. Mater. Chem. A* **2014**, *2*, 7960.
- [261] H. Li, K. Yu, C. Li, B. Guo, X. Lei, H. Fu, Z. Zhu, *J. Mater. Chem. A* **2015**, *3*, 20225.
- [262] a) A. Du, S. Sanvito, Z. Li, D. Wang, Y. Jiao, T. Liao, Q. Sun, Y. H. Ng, Z. Zhu, R. Amal, *J. Am. Chem. Soc.* **2012**, *134*, 4393; b) Z.-B. Liu, X. Zhao, X.-L. Zhang, X.-Q. Yan, Y.-P. Wu, Y.-S. Chen, J.-G. Tian, *J. Phys. Chem. Lett.* **2011**, *2*, 1972.
- [263] a) M.-Q. Yang, N. Zhang, Y.-J. Xu, *ACS Appl. Mater. Interfaces* **2013**, *5*, 1156; b) S. O.-B. Oppong, W. W. Anku, S. K. Shukla, E. S. Agorku, P. P. Govender, *J. Sol-Gel Sci. Technol.* **2016**, *80*, 38.
- [264] Y. Zhang, N. Zhang, Z.-R. Tang, Y.-J. Xu, *Phys. Chem. Chem. Phys.* **2012**, *14*, 9167.
- [265] J. Liu, Y. Liu, N. Liu, Y. Han, X. Zhang, H. Huang, Y. Lifshitz, S.-T. Lee, J. Zhong, Z. Kang, *Science* **2015**, *347*, 970.
- [266] S. Iijima, *Nature* **1991**, *354*, 56.
- [267] Y. T. Liang, B. K. Vijayan, O. Lyandres, K. A. Gray, M. C. Hersam, *J. Phys. Chem. Lett.* **2012**, *3*, 1760.
- [268] a) W. W. Anku, S. O.-B. Oppong, S. K. Shukla, E. S. Agorku, P. P. Govender, *Res. Chem. Intermed.* **2016**, *42*, 7231; b) W. W. Anku, S. O.-B. Oppong, S. K. Shukla, E. S. Agorku, P. P. Govender, *Prog. Nat. Sci.: Mater. Int.* **2016**, *26*, 354.
- [269] M. Li-Li, S. Hai-Zhen, Z. Yong-Gang, L. Yu-Lin, L. Jia-Lin, W. En-ke, Y. Ying, T. Ming, W. Jian-Bo, *Nanotechnology* **2008**, *19*, 115709.
- [270] W. Wang, P. Serp, P. Kalck, J. L. Faria, *J. Mol. Catal., A: Chem.* **2005**, *235*, 194.
- [271] G. Chai, C. Lin, J. Wang, M. Zhang, J. Wei, W. Cheng, *J. Phys. Chem. C* **2011**, *115*, 2907.
- [272] R. Long, *J. Phys. Chem. Lett.* **2013**, *4*, 1340.
- [273] M. T. Nguyen, C. K. Nguyen, T. M. P. Vu, Q. Van Duong, T. L. Pham, T. C. Nguyen, *Adv. Nat. Sci.: Nanosci. Nanotechnol.* **2014**, *5*, 045018.
- [274] L. E. Ratcliff, P. D. Haynes, *Phys. Chem. Chem. Phys.* **2013**, *15*, 13024.
- [275] H. Fu, T. Xu, S. Zhu, Y. Zhu, *Environ. Sci. Technol.* **2008**, *42*, 8064.
- [276] J. Yu, T. Ma, G. Liu, B. Cheng, *Dalton Trans.* **2011**, *40*, 6635.
- [277] Y. Cao, D. Wang, B. Liu, G. Yao, Y. Fu, X. Li, Z. Bi, *Int. J. Quantum Chem.* **2013**, *113*, 1440.
- [278] X. Bai, L. Wang, Y. Wang, W. Yao, Y. Zhu, *Appl. Catal., B* **2014**, *152*, 262.
- [279] J. Yu, T. Ma, S. Liu, *Phys. Chem. Chem. Phys.* **2011**, *13*, 3491.
- [280] C.-Y. Luo, W.-Q. Huang, L. Xu, Y.-C. Yang, X. Li, W. Hu, P. Peng, G.-F. Huang, *RSC Adv.* **2016**, *6*, 43228.
- [281] C.-Y. Luo, W.-Q. Huang, W. Hu, P. Peng, G.-F. Huang, *Dalton Trans.* **2016**, *45*, 13383.
- [282] C.-Y. Luo, W.-Q. Huang, L. Xu, Y.-C. Yang, X. Li, W. Hu, P. Peng, G.-F. Huang, *Phys. Chem. Chem. Phys.* **2016**, *18*, 2878.
- [283] K. Qi, R. Selvaraj, T. Al Fahdi, S. Al-Kindy, Y. Kim, G.-C. Wang, C.-W. Tai, M. Sillanpää, *Appl. Surf. Sci.* **2016**, *387*, 750.
- [284] W. Tu, Y. Zhou, Z. Zou, *Adv. Funct. Mater.* **2013**, *23*, 4996.
- [285] K. C. Kemp, H. Seema, M. Saleh, N. H. Le, K. Mahesh, V. Chandra, K. S. Kim, *Nanoscale* **2013**, *5*, 3149.
- [286] J. K. Wassei, R. B. Kaner, *Acc. Chem. Res.* **2013**, *46*, 2244.
- [287] P. Avouris, *Nano Lett.* **2010**, *10*, 4285.
- [288] J. Ito, J. Nakamura, A. Natori, *J. Appl. Phys.* **2008**, *103*, 113712.
- [289] T.-F. Yeh, J. Cihlář, C.-Y. Chang, C. Cheng, H. Teng, *Mater. Today* **2013**, *16*, 78.
- [290] H. Liu, Y. Liu, D. Zhu, *J. Mater. Chem.* **2011**, *21*, 3335.
- [291] T.-h. Ji, M. Sun, P. Han, *Carbon* **2014**, *70*, 319.
- [292] H. P. Boehm, R. Setton, E. Stumpp, *Carbon* **1986**, *24*, 241.
- [293] Q. Huang, S. Tian, D. Zeng, X. Wang, W. Song, Y. Li, W. Xiao, C. Xie, *ACS Catal.* **2013**, *3*, 1477.
- [294] Y. Ma, Y. Dai, W. Wei, C. Niu, L. Yu, B. Huang, *J. Phys. Chem. C* **2011**, *115*, 20237.
- [295] B. N. Joshi, H. Yoon, S.-H. Na, J.-Y. Choi, S. S. Yoon, *Ceram. Int.* **2014**, *40*, 3647.
- [296] X. Yang, H. Cui, Y. Li, J. Qin, R. Zhang, H. Tang, *ACS Catal.* **2013**, *3*, 363.
- [297] Y. Ma, Y. Dai, M. Guo, C. Niu, B. Huang, *Nanoscale* **2011**, *3*, 3883.
- [298] S. Zhuang, X. Xu, B. Feng, J. Hu, Y. Pang, G. Zhou, L. Tong, Y. Zhou, *ACS Appl. Mater. Interfaces* **2014**, *6*, 613.
- [299] W. Geng, X. Zhao, H. Liu, X. Yao, *J. Phys. Chem. C* **2013**, *117*, 10536.
- [300] Y. Yuan, X. Gong, H. Wang, *Phys. Chem. Chem. Phys.* **2015**, *17*, 11375.
- [301] W. Geng, H. Liu, X. Yao, *Phys. Chem. Chem. Phys.* **2013**, *15*, 6025.
- [302] H. Gao, X. Li, J. Lv, G. Liu, *J. Phys. Chem. C* **2013**, *117*, 16022.
- [303] a) R. Long, *ChemPhysChem* **2013**, *14*, 579; b) A. Du, Y. H. Ng, N. J. Bell, Z. Zhu, R. Amal, S. C. Smith, *J. Phys. Chem. Lett.* **2011**, *2*, 894.
- [304] X. Pengtao, T. Qing, Z. Zhen, *Nanotechnology* **2013**, *24*, 305401.
- [305] X. Li, H. Gao, G. Liu, *Comput. Theor. Chem.* **2013**, *1025*, 30.
- [306] F. Ren, J. Zhang, Y. Wang, W. Yao, *Phys. Chem. Chem. Phys.* **2016**, *18*, 14113.
- [307] Y.-C. Yang, L. Xu, W.-Q. Huang, C.-Y. Luo, G.-F. Huang, P. Peng, *J. Phys. Chem. C* **2015**, *119*, 19095.

- [308] L. Xu, W.-Q. Huang, L.-L. Wang, G.-F. Huang, P. Peng, *J. Phys. Chem. C* **2014**, *118*, 12972.
- [309] F. Nasrin, A. Serge, A. C. Paul, *Nanotechnology* **2014**, *25*, 305601.
- [310] S. Ayissi, P. A. Charpentier, N. Farhangi, J. A. Wood, K. Palotás, W. A. Hofer, *J. Phys. Chem. C* **2013**, *117*, 25424.
- [311] N. Yang, Y. Liu, H. Wen, Z. Tang, H. Zhao, Y. Li, D. Wang, *ACS Nano* **2013**, *7*, 1504.
- [312] Z. Ma, R. Sa, Q. Li, K. Wu, *Phys. Chem. Chem. Phys.* **2016**, *18*, 1050.
- [313] G. Eda, M. Chhowalla, *Adv. Mater.* **2010**, *22*, 2392.
- [314] O. C. Compton, S. T. Nguyen, *Small* **2010**, *6*, 711.
- [315] S. Liu, T. H. Zeng, M. Hofmann, E. Burcombe, J. Wei, R. Jiang, J. Kong, Y. Chen, *ACS Nano* **2011**, *5*, 6971.
- [316] S. Yu, X. Wang, Y. Ai, X. Tan, T. Hayat, W. Hu, X. Wang, *J. Mater. Chem. A* **2016**, *4*, 5654.
- [317] N. Li, G. Liu, C. Zhen, F. Li, L. Zhang, H. M. Cheng, *Adv. Funct. Mater.* **2011**, *21*, 1717.
- [318] D. R. Dreyer, S. Park, C. W. Bielawski, R. S. Ruoff, *Chem. Soc. Rev.* **2010**, *39*, 228.
- [319] T. Szabó, O. Berkesi, P. Forgó, K. Josepovits, Y. Sanakis, D. Petridis, I. Dékány, *Chem. Mater.* **2006**, *18*, 2740.
- [320] U. Hofmann, R. Holst, *Ber. Dtsch. Chem. Ges.* **1939**, *72*, 754.
- [321] G. Ruess, *Monatsh. Chem.* **1947**, *76*, 381.
- [322] W. Scholz, H. Boehm, *Z. Anorg. Allg. Chem.* **1969**, *369*, 327.
- [323] T. Nakajima, Y. Matsuo, *Carbon* **1994**, *32*, 469.
- [324] N. Greenwood, A. Earnshaw, *Chemistry of the Elements*, 2nd ed., Butterworth-Heinemann, London, UK **1997**.
- [325] A. Lurf, H. He, M. Forster, J. Klinowski, *J. Phys. Chem. B* **1998**, *102*, 4477.
- [326] K. A. Mkhoyan, A. W. Contryman, J. Silcox, D. A. Stewart, G. Eda, C. Mattevi, S. Miller, M. Chhowalla, *Nano Lett.* **2009**, *9*, 1058.
- [327] J. Kim, L. J. Cote, F. Kim, W. Yuan, K. R. Shull, J. Huang, *J. Am. Chem. Soc.* **2010**, *132*, 8180.
- [328] R. Vinoth, P. Karthik, C. Muthamizhchelvan, B. Neppolian, M. Ashokkumar, *Phys. Chem. Chem. Phys.* **2016**, *18*, 5179.
- [329] K. Krishnamoorthy, R. Mohan, S. J. Kim, *Appl. Phys. Lett.* **2011**, *98*, 244101.
- [330] E. S. Agorku, M. A. Mamo, B. B. Mamba, A. C. Pandey, A. K. Mishra, *Mater. Sci. Semicond. Process.* **2015**, *33*, 119.
- [331] X. Liu, L. Pan, Q. Zhao, T. Lv, G. Zhu, T. Chen, T. Lu, Z. Sun, C. Sun, *Chem. Eng. J.* **2012**, *183*, 238.
- [332] L. Liu, J. Liu, D. D. Sun, *Catal. Sci. Technol.* **2012**, *2*, 2525.
- [333] M. Wang, J. Huang, Z. Tong, W. Li, J. Chen, *J. Alloys Compd.* **2013**, *568*, 26.
- [334] F. Meng, J. Li, S. K. Cushing, M. Zhi, N. Wu, *J. Am. Chem. Soc.* **2013**, *135*, 10286.
- [335] X. An, J. C. Yu, J. Tang, *J. Mater. Chem. A* **2014**, *2*, 1000.
- [336] P. Wang, J. Wang, T. Ming, X. Wang, H. Yu, J. Yu, Y. Wang, M. Lei, *ACS Appl. Mater. Interfaces* **2013**, *5*, 2924.
- [337] X. Liu, L. Pan, Q. Zhao, T. Lv, G. Zhu, T. Chen, T. Lu, Z. Sun, C. Sun, *Chem. Eng. J.* **2012**, *183*, 238.
- [338] Y. Zhang, J. Tian, H. Li, L. Wang, X. Qin, A. M. Asiri, A. O. Al-Youbi, X. Sun, *Langmuir* **2012**, *28*, 12893.
- [339] L. Ye, J. Fu, Z. Xu, R. Yuan, Z. Li, *ACS Appl. Mater. Interfaces* **2014**, *6*, 3483.
- [340] L. Xu, W.-Q. Huang, L.-L. Wang, G.-F. Huang, *ACS Appl. Mater. Interfaces* **2014**, *6*, 20350.
- [341] S. Grimme, *J. Comput. Chem.* **2006**, *27*, 1787.
- [342] L. Xu, W.-Q. Huang, L.-L. Wang, Z.-A. Tian, W. Hu, Y. Ma, X. Wang, A. Pan, G.-F. Huang, *Chem. Mater.* **2015**, *27*, 1612.
- [343] H. J. Monkhorst, J. D. Pack, *Phys. Rev. B* **1976**, *13*, 5188.